Journal of Architectural Environment & Structural Engineering Research

Journal of Architectural Environment &Structural Engineering Research

Editor-in-Chief

Dr. Kaveh Ostad-Ali-Askari

Contents

ARTICLE

Failure Evaluation of Reinforced Concrete Beams Using Damage Mechanics and Classical Laminate Theory

José Mário Feitosa Lima[iD] **Geraldo José Belmonte dos Santos**[iD] **Paulo Roberto Lopes Lima**[*][iD]

State University of Feira de Santana, Technology Department, Feira de Santana, Bahia, 44030-900, Brazil

ABSTRACT

The prediction of the behavior of reinforced concrete beams under bending is essential for the perfect design of these elements. Usually, the classical models do not incorporate the physical nonlinear behavior of concrete under tension and compression, which can underestimate the deformations in the structural element under short and long-term loads. In the present work, a variational formulation based on the Finite Element Method is presented to predict the flexural behavior of reinforced concrete beams. The physical nonlinearity due cracking of concrete is considered by utilization of damage concept in the definition of constitutive models, and the lamination theory it is used in discretization of section cross of beams. In the layered approach, the reinforced concrete element is formulated as a laminated composite that consists of thin layers, of concrete or steel that has been modeled as elastic-perfectly plastic material. The comparison of numerical load-displacement results with experimental results found in the literature demonstrates a good approximation of the model and validates the application of the damage model in the Classical Laminate Theory to predict mechanical failure of reinforced concrete beam. The results obtained by the numerical model indicated a variation in the stress–strain behavior of each beam, while for under-reinforced beams, the compressive stresses did not reach the peak stress but the stress–strain behavior was observed in the nonlinear regime at failure, for the other beams, the concrete had reached its ultimate strain, and the beam's neutral axis was close to the centroid of the cross-section.

1. Introduction

The nonlinear numerical analysis of reinforced concrete structures has been implemented to predict both the reduction in stiffness with the increase in deformations, as well as the mechanism and process of failure [1]. The incorporation of nonlinear stress–strain models under tension and/or compression [2-4] has changed the constitutive equations of concrete.

*Corresponding Author:
Paulo Roberto Lopes Lima,
State University of Feira de Santana, Technology Department, Feira de Santana, Bahia, 44030-900, Brazil;
Email: lima.prl@pq.cnpq.br

Concrete is a cement-based composite material whose mechanical properties depend on the constituents and interfaces between them. Its behavior is defined by the pre-existence of pores, voids, inclusions, and microcracks prior to loading, which induces: (i) a post-cracking behavior of strain softening; (ii) progressive deterioration of the mechanical properties; (iii) volumetric expansion; (iv) induced anisotropy; (v) asymmetry in response to traction and compression; (iv) considered fragile in traction and quasi-ductile in compression. In contrast, reinforced concrete uses steel reinforcements embedded in the cementitious matrix to increase the strength and stiffness of the composite, primarily in the tension regions. Reinforced concrete exhibits an initially linear elastic behavior with a progressive increase in loading that progress to a nonlinear inelastic behavior induced by crack propagation and concrete crushing or steel yielding. Mathematical modeling of the nonlinear inelastic behavior of concrete, without considering creep, is typically based on plasticity theory, continuous damage theory, fracture mechanics, or a combination of these [5-12].

The isotropic Mazar damage model [13] allows the continuous representation of the structural model even after concrete cracking has generated good results in the modeling of reinforced concrete structures [14,15]. This model uses theories based on the mechanics of continuous damage that define the constitutive laws of concrete. Only one internal variable is required to apply this model and its evolution law is easily obtained by performing tensile and compression tests on the material.

In terms of discrete representation of reinforced concrete structures, the most common model for numerical analysis has been the use of the finite element method, wherein the concrete and reinforcement bars are modeled separately using two different types of elements. An additional approach has been used with the adoption of lamination, wherein the structural element is divided into several layers [2,16]. Based on the classical laminate theory, this model associates a specific type of material with each layer of the beam and considers the perfect adhesion between the layers. By monitoring the stresses and strains in each layer, the commencement of cracking in the concrete and the yielding of the reinforcement can be identified, thus resulting in a more realistic evaluation of the behavior of the structural elements of reinforced concrete.

The objective of this study is to assess the effectiveness of damage mechanics and classical lamination theory in the failure prediction of reinforced concrete beams. For this purpose, a variational formulation model was developed based on such theories and the principle of virtual work. Subsequently, it was applied using the finite element method (FEM) and the obtained results were compared with the experimental results reported in the literature.

2. Problem Formulation and Numerical Modeling

2.1 Materials Modelling

The model proposed by Mazars [13] is based on experimental evidence observed in the behavior of concrete under uniaxial tension and compression, wherein the material degrades owing to distributed microcracking caused by tensile stresses. In this model, the damage is represented by scalar variable D, whose evolution occurs only when an equivalent strain measure, $\tilde{\varepsilon}$, exceeds a threshold value, ε_{d0}, corresponding to the tensile strength of the concrete. The equivalent strain $\tilde{\varepsilon}$ represents the elongation local state and is given by:

$$\tilde{\varepsilon} = \sqrt{<\varepsilon_1>_+^2 + <\varepsilon_2>_+^2 + <\varepsilon_3>_+^2} \tag{1}$$

where $<\varepsilon_i>_+$ is the positive part of the elongation in the principal direction i and is defined as

$$<\varepsilon_i>_+ = \frac{1}{2}(\varepsilon_i + |\varepsilon_i|) = \begin{cases} \varepsilon_i, & if\ \varepsilon_i > 0 \\ 0, & if\ \varepsilon_i \leq 0 \end{cases} \tag{2}$$

In the pre-cracking phase ($\varepsilon \leq \varepsilon_{d0}$), the concrete exhibits linear elastic behavior. Whereas in the post-cracking phase, when the strain is greater than the elastic strain limit ($\varepsilon > \varepsilon_{d0}$), the concrete exhibits nonlinear elastic behavior when the initial elastic modulus E_0 is progressively damaged.

Thus, the uniaxial stress–strain behavior of concrete can be established by:

$$\sigma = \begin{cases} E_o\ \varepsilon, & \varepsilon \leq \varepsilon_{d0} \\ (1 - D)\ E_o\varepsilon, & \varepsilon > \varepsilon_{d0} \end{cases} \tag{3}$$

In Equation (3), the damage parameter D varies between 0 (when $\varepsilon \leq \varepsilon_{d0}$) and 1 (when the material is completely damaged), as expressed by (see [14,15]):

$$D = \alpha_T D_T + \alpha_C D_C \tag{4}$$

with

$$\alpha_T = \frac{\sum_i <\varepsilon_{T_i}>_+}{\sum_i <\varepsilon_{T_i}>_+ + \sum_i <\varepsilon_{C_i}>_+} \tag{5}$$

$$\alpha_C = \frac{\sum_i <\varepsilon_{C_i}>_+}{\sum_i <\varepsilon_{T_i}>_+ + \sum_i <\varepsilon_{C_i}>_+} \tag{6}$$

$$D_T(\tilde{\varepsilon}) = 1 - \frac{\varepsilon_{d0}(1-A_T)}{\tilde{\varepsilon}} - \frac{A_T}{\exp[B_T(\tilde{\varepsilon}-\varepsilon_{d0})]}, \text{ and} \tag{7}$$

$$D_C(\tilde{\varepsilon}) = 1 - \frac{\varepsilon_{d0}(1-A_C)}{\tilde{\varepsilon}} - \frac{A_C}{exp[B_C(\tilde{\varepsilon}-\varepsilon_{d0})]} \tag{8}$$

where $\alpha_T + \alpha_C = 1$, ε_{T_i} and ε_{C_i} are the components of the principal strains determined by the positive and nega-

tive parts, respectively. The values A_T, B_T, A_C, B_C and ε_{d0} are the experimental parameters obtained from the material tests.

For the reinforcing steel bars, the linear elastic behavior between the stress and strain before yield deformation is assumed to be $\sigma_s = E_s\varepsilon$, $if\ \varepsilon < \varepsilon_y$, where E_s is the elastic modulus of the steel. After yielding $\varepsilon \geq \varepsilon_y$, the stress is assumed to be constant, $\sigma_s = f_y$, where f_y is the yielding stress of the steel and exhibits linearly elastic–perfectly plastic behavior.

In this study, the cross section of the beams was discretized in NC layers of thickness h_k (k=1,..., NC), as shown in Figure 1.
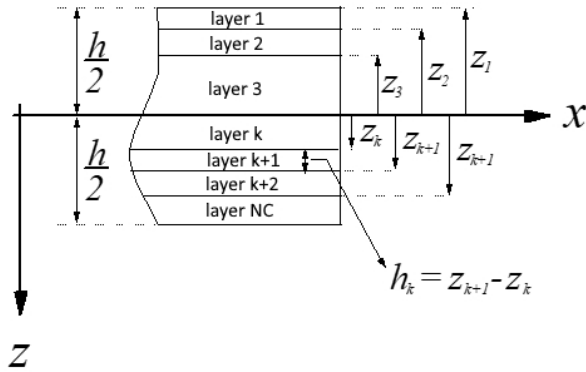
Figure 1. Discretization of the laminated beam

Classical laminate theory establishes that the laminae that form the laminate are in a plane stress state. In this context, and based on the generalized Hooke's law for homogeneous and isotropic materials, the following relationship between stresses and strains in each layer of the laminate is valid [16].

$$\begin{Bmatrix} \sigma_x \\ \sigma_y \\ \tau_{xy} \end{Bmatrix} = \begin{bmatrix} Q_{11}^{(k)} & Q_{12}^{(k)} & 0 \\ Q_{12}^{(k)} & Q_{22}^{(k)} & 0 \\ 0 & 0 & Q_{66}^{(k)} \end{bmatrix} \begin{Bmatrix} \varepsilon_x \\ \varepsilon_y \\ \gamma_{xy} \end{Bmatrix} \tag{9}$$

where the quantities $Q_{11}^{(k)}, Q_{12}^{(k)}, Q_{22}^{(k)}$ and $Q_{66}^{(k)}$ are the mechanical constants related to the engineering properties of the layer material, as defined below.

$$Q_{11}^{(k)} = Q_{22}^{(k)} = \left(\frac{E}{1-v^2}\right)^{(k)} \tag{10}$$

$$Q_{12}^{(k)} = \left(\frac{vE}{1-v^2}\right)^{(k)}, \text{ and} \tag{11}$$

$$Q_{66}^{(k)} = \left(\frac{E}{2(1+v)}\right)^{(k)} = (G)^{(k)} \tag{12}$$

where E and G represent the longitudinal and transverse moduli of elasticity of the material, respectively, which make up the layer of the laminate; and v is Poisson's ratio.

In the formulation proposed here, the elastic modulus

present in quantities $Q_{11}^{(k)}, Q_{12}^{(k)}, Q_{22}^{(k)}$ and $Q_{66}^{(k)}$ incorporates the damage that occurs in the concrete layers and is given by Equations (4)–(8). When the layer is steel, the stress–strain relationship incorporates plastic strain after the yield limit.

The classical laminate theory is typically developed only for laminates formed by orthotopic or isotropic materials [16]. However, this theory can be considered as an extension of the classical theory to address problems involving materials subject to damage and plasticity.

2.2 Internal Stress Resultants in the Laminated Section

The model used in the study, which appears in the Euler–Bernoulli Beam theory in a single stress component σ_x in Equation (9) used for the analysis of beams, is believed to have only one non-zero strain component ε_x, as given below.

$$\sigma_x = Q_{11}^{(k)}\varepsilon_x \tag{13}$$

The internal stresses in the generic cross-section of the laminate of area A are related by the following equations.

$$N = \int_A \sigma_x\, dA = b \int_{-h/2}^{h/2} \sigma_x dz \tag{14}$$

$$M = \int_A \sigma_x\, z dA = b \int_{-h/2}^{h/2} \sigma_x z dA \tag{15}$$

where N denotes the normal force; M denotes the bending moment; b denotes the width of the section; and h denotes its height.

For a laminated cross section, as shown in Figure 1, the evaluation of these internal stress resultants is performed by adding the contribution from each lamina; in this process, different materials are considered. With the development of the addition, we obtain Equations (16) and (17), which are compact expressions of the resultants.

$$N = A_{11}\frac{\partial u_0}{\partial x} - B_{11}\frac{\partial^2 w_0}{\partial x^2} \tag{16}$$

$$M = B_{11}\frac{\partial u_0}{\partial x} - D_{11}\frac{\partial^2 w_0}{\partial x^2} \tag{17}$$

where

$$A_{11} = b\sum_{k=1}^{NC} Q_{11}^{(k)}(z_{k+1} - z_k) \tag{18}$$

$$B_{11} = \frac{b}{2}\sum_{k=1}^{NC} Q_{11}^{(k)}(z_{k+1}^2 - z_k^2) \tag{19}$$

$$D_{11} = \frac{b}{3}\sum_{k=1}^{NC} Q_{11}^{(k)}(z_{k+1}^3 - z_k^3) \tag{20}$$

The quantities A_{11}, B_{11}, and D_{11} are associated with the term [1, 1] of the matrices of extensional stiffness [A], bending stiffness [B], and coupling [D], respectively, as they are referred to in the classical laminate theory [16]. However, note that Equations (18)–(20) incorporate the

width of section b of the beam, which is not present in the equations of classical laminate theory.

2.3 Principle of Virtual Works

In this study, FEM was used to model the laminated beam, and the principle of virtual work was used to write equilibrium equations and transform the continuous problem into a discrete problem.

Given that the structural system will be in equilibrium, if the total virtual work of the applied forces is zero, for any compatible virtual (and infinitesimal) displacement, the initial problem is determining the virtual work done by the internal forces and the virtual work done by external forces.

The virtual work done by the internal forces for the problem is given by:

$$\delta W_{int} = \int_V \sigma_x \delta \varepsilon_x dV \tag{21}$$

where $\delta \varepsilon_x$ is the variation in the strain component ε_x; and V is the volume of the beam.

For the laminated section shown in Figure 1, we obtain the following.

$$\delta W_{int} = \int_0^L \left[\left(A_{11} \frac{\partial u_0}{\partial x} - B_{11} \frac{\partial^2 w_0}{\partial x^2} \right) \delta \left(\frac{\partial u_0}{\partial x} \right) - \left(B_{11} \frac{\partial u_0}{\partial x} \right. \right.$$
$$\left. \left. - D_{11} \frac{\partial^2 w_0}{\partial x^2} \right) \delta \left(\frac{\partial^2 w_0}{\partial x^2} \right) \right] dx \tag{22}$$

The virtual work done by the external forces, assuming that the loads are applied directly to the axis of the structure to produce bending, is given by:

$$\delta W_{ext} = \int_0^L \left[p(x) \delta u_0 + q(x) \delta w_0 \right] dx$$
$$+ \left[\bar{F}_x \delta u_0 + \bar{F}_z \delta w_0 - \bar{M} \delta \left(\frac{\partial w_0}{\partial x} \right) \right]_0^L \tag{23}$$

where $p(x)$ and $q(x)$ represent the distributed loads of the domain according to the axial x axis and transverse z axis, respectively; $\bar{F}_x$ and $\bar{F}_z$ represent the forces applied at the beam ends ($x = 0$ and $x = L$), respectively; and $\bar{M}$ represents the external moments applied at the same ends.

By applying the equilibrium condition imposed by the principle of virtual work (PTV), that is, $\delta W_{int} = \delta W_{ext}$, the differential equations of the problem can be instituted, previously making the variations of displacements in the domain portions in Equations (22) and (23) through integration by parts.

This result in the system of differential equations associated with the model:

$$A_{11} \frac{\partial^2 u_0}{\partial x^2} - B_{11} \frac{\partial^3 w_0}{\partial x^3} = - p(x) \quad \text{or} \quad \frac{\partial N}{\partial x} = - p(x) \tag{24}$$

$$B_{11} \frac{\partial^3 u_0}{\partial x^3} - D_{11} \frac{\partial^4 w_0}{\partial x^4} = q(x) \quad \text{or} \quad \frac{\partial^2 M}{\partial x^2} = q(x) \tag{25}$$

Because of the application of PTV, the following

boundary conditions are extracted at $x = 0$ and $x = L$, inherent to the model:

$$u_0 = \bar{u}_0 \text{ and } \delta u_0 = \delta \bar{u}_0 \qquad \text{or} \qquad N = \bar{F}_x \tag{26}$$

$$w_0 = \bar{w}_0 \text{ and } \delta w_0 = \delta \bar{w}_0 \qquad \text{or} \qquad Q = \bar{F}_z \tag{27}$$

$$\frac{\partial w_0}{\partial x} = \frac{\partial w_0}{\partial x} \text{ and } \delta \left(\frac{\partial w_0}{\partial x} \right) = \delta \left(\frac{\partial w_0}{\partial x} \right) \quad \text{or} \quad M = \bar{M} \tag{28}$$

where Q is the shear force in the section obtained from the equilibrium of the differential element of the beam.

$$Q = \frac{\partial M}{\partial x} = B_{11} \frac{\partial^2 u_0}{\partial x^2} - D_{11} \frac{\partial^3 w_0}{\partial x^3} \tag{29}$$

2.4 Discretization by the Finite Element Method

2.4.1 Determination of the Stiffness Matrix

Herein, the classical beam element was chosen for treatment using FEM for formulation developed in the previous subsections [17]. This element is delimited by two nodes at its ends, with three degrees of freedom at each of these nodes: u_0, w_0, and $\frac{\partial w_0}{\partial x}$. The interpolation functions used to represent the displacements along the finite element of length L_{el} were cubic polynomials for $w_0 = w_0(x)$ and linear polynomials for $u_0 = u_0(x)$. Finally, the rotation $\frac{\partial w_0}{\partial x}$ was obtained by deriving from $w_0(x)$.

The FEM application generates a system of nodal equilibrium equations of type

$$[K]\{D\} = \{F\} \tag{30}$$

where $[K]$ is the global stiffness matrix of the structure, a function of both the geometry of the beam and the mechanical properties of the materials, and is given by the assembly of elements, as shown in Equation (31); $\{F\}$ is the global vector of loads, containing the equivalent nodal loads acting on the structure; and $\{D\}$ is the vector of nodal displacements, obtained by solving the system of Equations (30).

$$[K] = \sum_1^{NE} [k_{el}] \tag{31}$$

where NE is the number of finite elements defined in the beam discretization; and $[k_{el}]$ is the stiffness matrix of the beam element, which is given by

$$[k_{el}] = \begin{bmatrix} \frac{A_{11}}{L_{el}} & 0 & -\frac{B_{11}}{L_{el}} & -\frac{A_{11}}{L_{el}} & 0 & \frac{B_{11}}{L_{el}} \\ 0 & \frac{12D_{11}}{L_{el}^3} & \frac{6D_{11}}{L_{el}^2} & 0 & -\frac{12D_{11}}{L_{el}^3} & \frac{6D_{11}}{L_{el}^2} \\ -\frac{B_{11}}{L_{el}} & \frac{6D_{11}}{L_{el}^2} & \frac{4D_{11}}{L_{el}} & \frac{B_{11}}{L_{el}} & -\frac{6D_{11}}{L_{el}^2} & \frac{2D_{11}}{L_{el}} \\ -\frac{A_{11}}{L_{el}} & 0 & \frac{B_{11}}{L_{el}} & \frac{A_{11}}{L_{el}} & 0 & -\frac{B_{11}}{L_{el}} \\ 0 & -\frac{12D_{11}}{L_{el}^3} & -\frac{6D_{11}}{L_{el}^2} & 0 & \frac{12D_{11}}{L_{el}^3} & -\frac{6D_{11}}{L_{el}^2} \\ \frac{B_{11}}{L_{el}} & \frac{6D_{11}}{L_{el}^2} & \frac{2D_{11}}{L_{el}} & -\frac{B_{11}}{L_{el}} & -\frac{6D_{11}}{L_{el}^2} & \frac{4D_{11}}{L_{el}} \end{bmatrix} \tag{32}$$

During the process of applying loads on the structural element, the matrix $[k_{el}]$ can be different even for ele-

ments of the same length L_{el} because the cracking process of the concrete or the yielding of the reinforcement causes the damage variable to assume different values along the length or height of the beam.

2.4.2 Nonlinear Analysis

To reach the final equilibrium solution, incremental application of external loads was performed to obtain an initial (predicted) solution, followed by an iterative Newton–Raphson using force or displacement control process. Table 1 summarizes the flowchart of the program.

2.5 Model Validation

The experimental results obtained by Álvares [15] were used to validate the proposed model. Reinforced concrete beams with different reinforcement ratios were experimentally investigated to evaluate their failure form when subjected to a four-point bending test. The experimental test of the beams was performed with load control such that the test was interrupted when the breaking load was reached.

The beams evaluated by Álvares [15] had a rectangular section measuring 120 mm × 300 mm, with a span of 2400 mm and loads located 800 mm from the support, as shown in Figure 2a and 2b.

The reinforcement rate of the beams was varied such that three types of failures, namely flexural tension failure (under-reinforced section), flexural compression

failure (over-reinforced section), and simultaneous failure (optimized section), could be evaluated. The upper reinforcement of all beams consisted of two bars with a diameter of 5 mm. The lower reinforcement varied based on the type of failure expected for the beam: i) for the under-reinforced section beam (Figure 2b), three bars with a diameter of 10 mm were used ($A_s = 236$ mm^2); ii) for the optimized section beam (Figure 2c), five bars with a diameter of 10 mm were used ($A_s = 393$ mm^2); iii) for the over-reinforced section beam (Figure 2d), seven bars with a diameter of 10 mm were used ($A_s = 550$ mm^2). For beam reinforcement, the following properties were assumed for steel: $E_s = 196$ GPa, $f_y = 500$ MPa, and $f_u = 500$ MPa.

For concrete modeling, an elastic modulus of 29.2 GPa and the following parameters necessary for the Mazar damage model, defined by Álvares [15], were used. $A_t = 995$, $B_t = 8000$, $A_c = 0.85$, $B_c = 1620$ and $\varepsilon_{d0} = 0.00007$. Additionally, a Poisson's ratio of 0.2 was assumed.

A convergence study (verification process) of the discretization parameters of the load–displacement solution was performed to determine the finite element mesh of the beams by varying the number of layers (10, 20, and 40 layers) of the cross section, the number of elements for the length of the beams (12, 24, 36, and 48 elements), the initial load step (0.5, 1.0, and 2.0 kN), and the tolerance of the iterative process (10^{-3}, 10^{-4}, and 10^{-6}). Therefore, the investigation recommended for the simulation of the three beams were a discretization of 20 layers and 36 elements, an initial load step of 1 kN and tolerance of 10^{-6}.

Table 1. Iterative process of obtaining a solution

Pre-cracking phase (D = 0)	Post-cracking phase (D > 0)
	1. Calculation of the stiffness matrix in relation to the last equilibrium configuration using displacements, strains, stresses, and the updated damage variable;
	2. Update load from load increment {ΔF};
	3. Solve the system of Equation (30);
1. Calculation of the stiffness matrix;	4. Check convergence through the unbalanced force (external forces minus internal forces);
2. The load is updated from the load increment {ΔF};	5. If there is no convergence, the stiffness of the structure must be updated and then the increment of the nodal displacements {ΔD} must be calculated
3. Solve the system of Equation (30);	through the unbalance force. Subsequently, the displacements ({ΔD} + {D}) and
4. Return to step 1;	the damage variable are updated. Finally, the unbalanced force is updated and the convergence is verified (external force minus internal force). Repeat this process until the solution converges to that charge level.
	6. After convergence, go back to step 1.
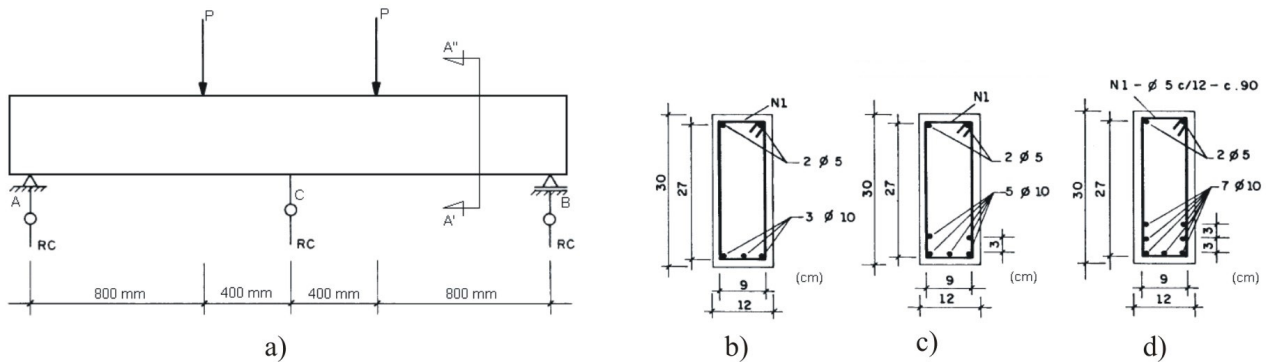
Figure 2. Experimental setup [15]: a) four-point bending test; b) under-reinforced beam; c) optimized beam; d) over-reinforced beam.

3. Results and Discussion

For the three types of beams, Figures 3~5 show the force–displacement curves obtained experimentally by Álvares [15] and the respective numerical results obtained from the proposed model. The experimentally acquired force–displacement curves exhibited the typical behavior of reinforced concrete beams subjected to bending failure, along with the identification of three stages (Figure 3). In Stage I, the concrete was undamaged, and the stiffness of the EI_I beams was because of the combined action of concrete and steel. The cracking of concrete indicates the end of this stage. The cracking load is defined by the tensile strength of the concrete.

In stage II, the curve initially exhibits nonlinear behavior that is characterized by the appearance of multiple cracks on the lower face of the beam. Gradually, stress is transferred to the steel bars, which provide the tensile strength of the beam. As the load increases, a second linear section is formed whose slope represents the stiffness EI_{II} of the cracked beam and is defined primarily by the reinforcement rate. However, the cracked concrete can contribute to the stiffness in a phenomenon called the tension-stiffening effect [18].

Stage III begins with a further reduction in the stiffness and a trend to stabilize the force until the beam fails. The reinforcement rate of the beam affects the force and displacements that define the beginning and end of stage III, which can lead to three types of failure associated with deformations in steel and concrete at the instant of beam collapse.

For stages I and II, a good approximation between the experimental load–displacement curves and the curves obtained using the proposed model, wherein the damage model is associated with the classical theory of laminates, can be confirmed by comparing the numerical results with the experimental results. However, the experimental curve presents an ultimate displacement during the beam test that is smaller than that predicted by the numerical result. This is because the load control used in the experiment halts the test when the maximum load is reached.

In the numerical model, taking the limits of deformation presented in Figure 6 as a reference, the beam failure was established by monitoring the strains in the most compressed concrete layer and in the most stressed steel layer. The ultimate limit states of a reinforced concrete beam can be established when the strain in the concrete reaches a value $\varepsilon_{cu}= 0.35\%$ because of compression failure, and/or by tensile failure when the strain in the steel reaches a value $\varepsilon_{su}= 1.00\%$ caused by crushing the compressed section. Balanced beams fail because of crushing of the compressed region; however, the strain in the steel is equal to or less than the yield strain ε_{sy}. When the beam cross-section and reinforcement ratio are optimally designed, failure occurs simultaneously in the top compressed layer and the most tensioned reinforcement section.

The proposed numerical model allows for the monitoring of the strains of the materials of the beam and the identification of the failure mechanism, as shown in Figure 7. In the over-reinforced beam, failure occurs by crushing the compressed region. This beam has the highest failure load, of the order of 73 kN, but a lower total displacement than the other beams analyzed. For the under-reinforced beam, the maximum load obtained was 81% lower than the load observed for the over-reinforced beam, and the deformation was 1.2 times greater. The optimized beam presents a load 46% less than the load observed for the over-reinforced beam, but with a deformation 1.3 times greater. In addition, this beam presents the best use of materials, which contributes to the reduction of energy consumption and non-renewable materials, thereby increasing the sustainability of the structures.
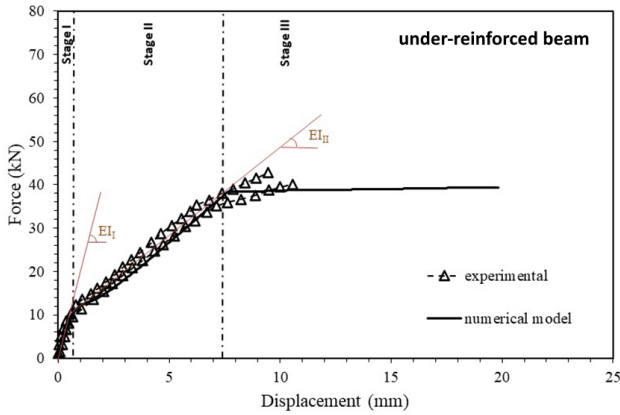
Figure 3. Flexural behavior of under-reinforced beam
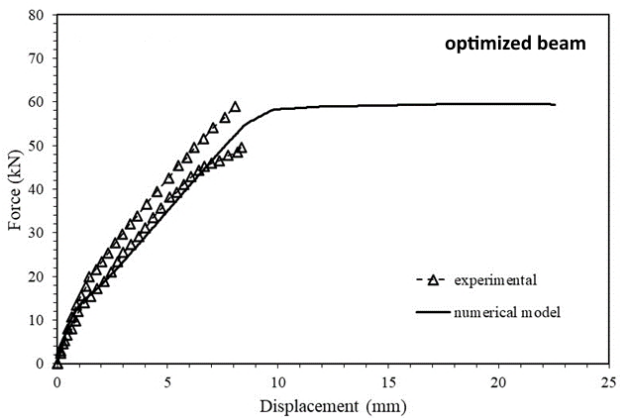
Figure 4. Flexural behavior of optimized beam
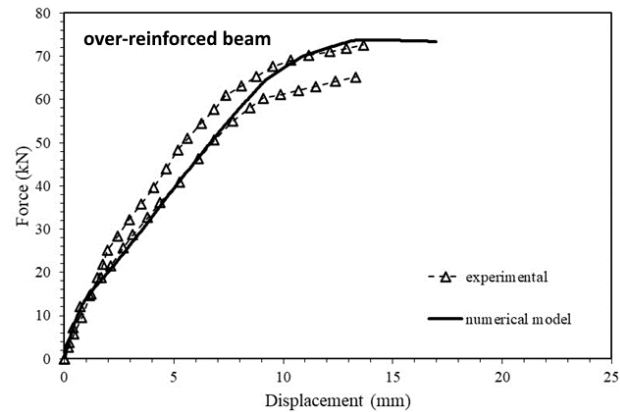
Figure 5. Flexural behavior of over-reinforced beam

The results obtained by the numerical model indicated a variation in the stress–strain behavior of each beam, as shown in Figure 8. For under-reinforced beams, the

compressive stresses did not reach the peak stress but the stress–strain behavior was observed in the nonlinear regime at failure, thus indicating the appearance of damage to the stiffness of the concrete. As the strains in the reinforcement reached their maximum value, the neutral axis approached the upper surface of the beam section. For the other beams, the concrete had reached its ultimate strain, and the beam's neutral axis was close to the centroid of the cross-section.
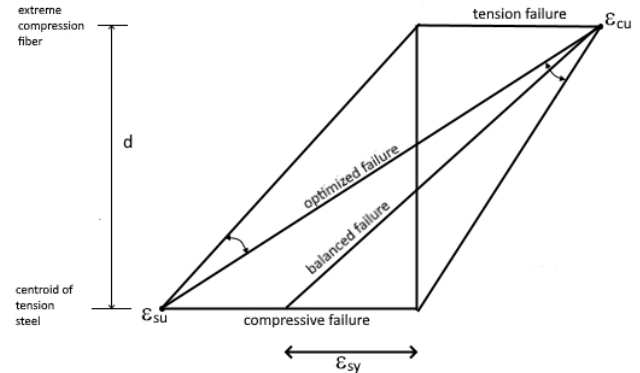
Figure 6. Strain limits for steel and concrete in the beam cross section
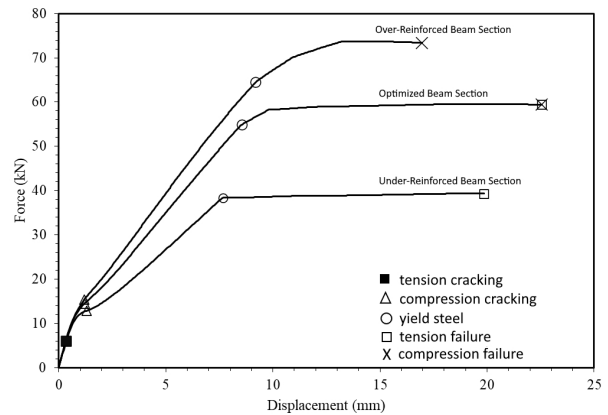
Figure 7. Theoretical identification of limiting strains of steel and concrete

Evidently, the proposed model for the behavior of tensioned concrete considers the contribution of cracking concrete (below the neutral axis), in contrast to design codes for reinforced concrete structures, even though the tensile stress value is low when comparing the stresses in the reinforcement and even in the compressed concrete.
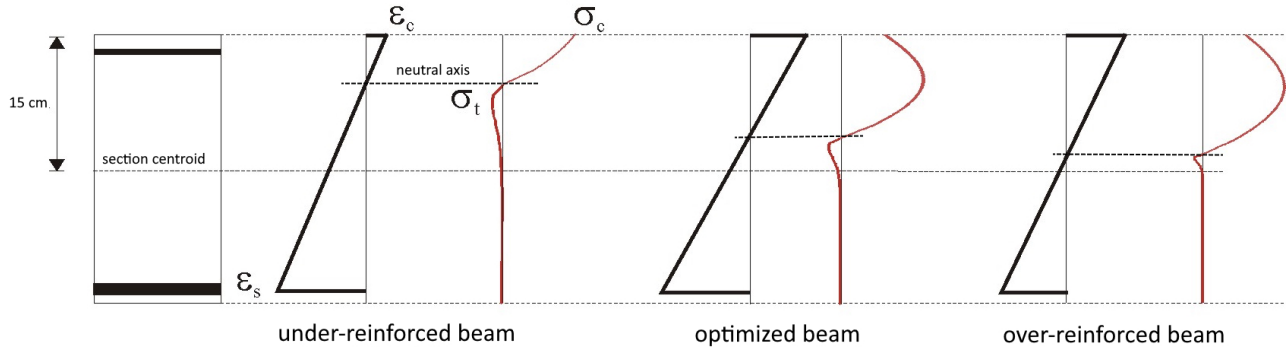
Figure 8. Stress–strain diagrams of concrete at failure of beam.

The variation in the stress–strain behavior is a function of the evolution of the damage parameter. As established by Equation (3), when the deformations exceed the limit value, ε_{d0}, there is a gradual reduction in the stiffness of the beam owing to cracking of the concrete. Figure 9 shows the variation in the damage parameter $(1-D_c)$ for the three types of beams investigated, with the increase in the vertical displacement of the beam. Initially, the value of $(1-D_c)$ was equal to unity because there was no damage to the compressed concrete. With increasing displacement, a reduction in this parameter was verified; however, it was affected by the reinforcement ratio of the beam. At failure, compression damage of approximately 60% was observed for under-reinforced beams, and the damage was approximately 80% for the optimized and over-reinforced beams.

Figure 9. Variation in the damage parameter with increase in the vertical displacement of the beams.

4. Limitations of the Study

The model used in this study, within the scope of static loading, ignores shear and geometric nonlinearity effects. Furthermore, the Mazars damage model is elastic and is not appropriate for situations of cyclic loadings, which is not the case in the pre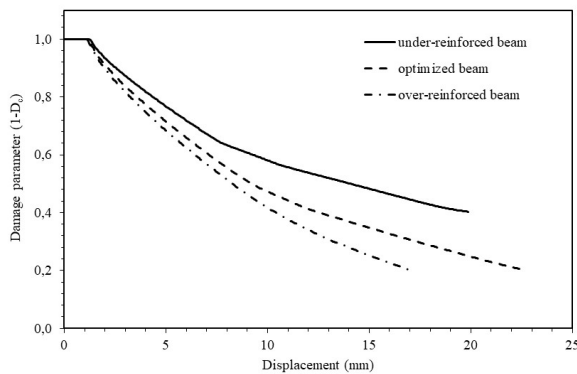sent study. However, the order of magnitude of the maximum transverse displacement of the beam with respect to the height is small, thus justifying the geometric linear analysis. The failure modes of the beams did not include shear failures.

5. Conclusions

The proposed model combines the classic theory of laminates and the Mazars damage model. By using FEM, it was able to evaluate the flexural behavior of reinforced concrete beams up to the failure of these elements for different rates of flexural using numerical simulation of the reinforced concrete beams under four-point bend tests. This was possible because the strategy of incorporating in the finite elements, the lamination of the transverse section, and the physical nonlinearity of the materials by continuous damage mechanics allowed the following of the stress and strain state of each layer of material, whether concrete (with its progressive cracking) or the reinforcement (even in the yielding).

Therefore, despite the relative simplicity of the proposed model, its potential to predict the behavior of reinforced concrete beams under bending was demonstrated, thereby allowing a precise identification of deformations and rupture criteria. The numerical model allowed the identification of the failure form of each type of reinforced concrete beam analyzed, through the prediction of the neutral line variation and the determination of the stress-strain behavior. In this way, the model can be used to predict the behavior of structural elements subjected to bending and lead to optimized designs, with greater safety and lower cost.

Author Contributions

JMFL: methodology, numerical modelling, formal analysis, writing - original draft; PRLL: conceptualization, investigation, data curation, formal analysis, writing - review & editing; GJBS: numerical modelling, formal

analysis, writing - original draft.

Conflict of Interest

Funding

References

[1] Wang, T., Hsu, T., 2001. Nonlinear finite element analysis of concrete structures using new constitutive models. Computer& Structures. 79, 2781-2791.

[2] Assan, A., 2002. Nonlinear analysis of reinforced concrete cylindrical shells. Computer&Structures. 80, 2177-2184.

[3] Tao, X., Phillips, D., 2005. A simplified isotropic damage model for concrete under bi-axial stress states. Cement & Concrete Composites. 27, 716-726.

[4] Mazars, J., Kotronis, P., Ragueneau, F., et al., 2006. Using multifiber beams to account for shear and torsion. Applications to concrete structural elements. Computer Methods in Applied Mechanics and Engineering. 195, 7264-7281.

[5] Butean, C., Heghes, B., 2020. Flexure Behavior of a two layer reinforced concrete beam. Procedia Manufacturing. 46, 110-115.

[6] Liu, C., Yang, Y., Wang, J., et al., 2020. Biaxial reinforced concrete constitutive models for implicit and explicit solvers with reduced mesh sensitivity. Engineering Structures. 219, 110880.

[7] Tjitradi, D., Eliatun, E., Taufik, S., 2017. 3D ANSYS numerical modeling of reinforced concrete beam behavior under different collapsed mechanisms. International Journal of Mechanics and Applications. 7(1), 14-23.

[8] Gorgogianni, A., Elias, J., Le, J.L., 2020. Mechanism-based energy regularization in computational modeling of quasibrittle fracture. Journal of Applied Mechanics. 87(9), 091003.

[9] Arruda, M.R.T., Pacheco, J., Castro, L.M.S., et al.,

2022. A modified mazars damage model with energy regularization. Engineering Fracture Mechanics. 259, 108129.

[10] Carrera, E., Augello, R., Pagani, A., et al., 2021. Component-wise approach to reinforced concrete structures. Mechanics of Advanced Materials and Structures. 1-19.

[11] Arruda, M.R.T., Castro, L.M.S., 2021. Non-linear dynamic analysis of reinforced concrete structures with hybrid mixed stress finite elements. Advances Engineering Software. 153, 102965.

[12] Leone, F.A., Justusson, B.P., 2020. Effects of characteristic element length on fracture energy dissipation in continuum damage mechanics models. Journal of Composites Materials. 55(24), 3551-3566.

[13] Di Prisco, M., Mazars, J., 1996. Crush-crack': a non-local damage model for concrete. Mechanics of Cohesive-frictional Materials. An International Journal on Experiments, Modelling and Computation of Materials and Structures. 1(4), 321-347.
DOI: https://doi.org/10.1002/(SICI)1099-1484 (199610)1:4<321::AID-CFM17>3.0.CO;2-2

[14] Mazars, J., Lemaitre, J., 1985. Application of Continuous Damage Mechanics to Strain and Fracture Behavior of Concrete. Shah, S.P. (eds) Application of Fracture Mechanics to Cementitious Composites. NATO ASI Series, vol 94. Springer, Dordrecht.
DOI: https://doi.org/10.1007/978-94-009-5121-1_17

[15] Alva, G.M.S., El Debs, A.L.H.C., Kaminski Jr, J., 2010. Nonlinear analysis of reinforced concrete structures in design procedures: application of lumped dissipation models. Revista IBRACON de Estruturas e Materiais. 3, 149-178.
DOI: https://doi.org/10.1590/S1983-41952010000200003

[16] Reddy, J.N., 2004. Mechanics of laminated composite plates and shells: theory and analysis. CRC Press. USA. pp. 831.

[17] Cook, R.D., Malkus, D.S., Plesha, M.E., et al., 2002. Concepts and applications of finite element analysis. John Wiley & Sons. Inc. USA. pp. 719.

[18] Martins, M.P., Rangel, C.S., Amario, M., et al., 2020. Modelling of tension stiffening effect in reinforced recycled concrete. Revista Ibracon de Estruturas e Materiais. 13, 1-21.

REVIEW

Dynamic Reliability Assessment of Heavy Vehicle Crossing a Prototype Bridge Deck by Using Simulation Technology and Health Monitoring Data

Yinghua Li[1*]   Junyong He[2]   Xiaoqing Zeng[3]   Yanxing Tang[4]

1. Shixing County Administrative Service Center, Shixing, Shaoguan, Guangdong, 512500, China
2. Guangdong College of Industry and Commerce, No. 1O98, Guangzhou North Road, Tianhe, Guangzhou, Guangdong, China
3. Shixing County Statistics Bureau, Shixing, Shaoguan, Guangdong, 512500, China
4. Shixing County Hospital of Traditional Chinese Medicine, Shixing, Shaoguan, Guangdong, 512500, China

ABSTRACT

Overloads of vehicle may cause damage to bridge structures, and how to assess the safety influence of heavy vehicles crossing the prototype bridge is one of the challenges. In this report, using a large amount of monitored data collected from the structural health monitoring system (SHMS) in service of the prototype bridge, of which the bridge type is large-span continuous rigid frame bridge, and adopting FEM simulation technique, we suggested a dynamic reliability assessment method in the report to assess the safety impact of heavy vehicles on the prototype bridge during operation. In the first place, by using the health monitored strain data, of which the selected monitored data time range is before the opening of traffic, the quasi dynamic reliability around the embedded sensor with no traffic load effects is obtained; then, with FEM technology, the FEM simulation model of one main span of the prototype bridge is built by using ANSYS software and then the dynamic reliability when the heavy vehicles crossing the prototype bridge corresponding to the middle-span web plate is comprehensively analyzed and discussed. At last, assuming that the main beam stress state change is in the stage of approximately linear elasticity under heavy vehicle loads impact, the authors got the impact level of heavy vehicles effects on the dynamic reliability of the prototype bridge. Based on a large number of field measured data, the dynamic reliability value calculated by our proposed methodology is more accurate. The method suggested in the paper can do good for not only the traffic management but also the damage analysis of bridges.

*Corresponding Author:
Yinghua Li,
Shixing County Administrative Service Center, Shixing, Shaoguan, Guangdong, 512500, China;
Email: lyh304236@163.com*

1. Introduction

Heavy vehicle in many countries, especially in developing countries, is a widespread problem resulting in early damage of the bridge and brings in huge economic losses. Here, we take China as an example. By 2020, China's total expressway mileage is up to 161,000 km. Due to the reforms and opening up as well as the deepening of China's market economy, the states have heavily increased investment in infrastructure, bringing the transportation sector to a new stage. However, a variety of problems, such as increase in traffic, loads due to heavy-duty vehicles, increasing speed of the vehicles as well as increased carrying capacity, presents the transport sector with "high-volume, heavy and channel traffic" challenges. The increasing heavy trucks cause a cumulative growth in the standard axle load and lead to serious damage of the roads and bridges. Urban roads and bridges carrying these heavy transport regularly induce the bridge structures and its components to withstand large dynamic load and frequent load times. Although the stress level is far below the ultimate strength or yield limit of materials used in the bridges such as steel, concrete etc., it often causes sudden and unexpected destruction.

As for the impact of overweight vehicles on bridge safety, many scholars around the world have conducted extensive research. Kirkegaard P H et al. [1] considered the vehicle load dynamic amplification on minor highway bridges for evaluating the safety of the bridge structure load carrying capacity. Zhao Yu et al. [2] elaborate the evaluation steps, checking principles, checking methods and traffic management measures of the overweight vehicles passing through the bridge deck, which provides the way for evaluating the overweight vehicles passing through the bridge. Chang Hao et al. [3] take reinforcement measures seriously, of which the aim is to cooperate with overweight vehicles crossing the bridge, and resolutely put an end to all kinds of major accidents to ensure the smooth flow of the road. Jiang H et al. [4] established a bridge model with finite element software and the process that heavy vehicle pass through the bridge was simulated, and finally the safety margin of the bridge was evaluated on the basis of bearing capacity analysis. Na H S et al. [5] identified the dynamic characteristics with vehicle-impact loading and analyzed the behaviors of U-channel segmental concrete bridge (UCB) system. Yu Xiaofei [6] presents the harm of heavy vehicles to bridges, and puts forward relevant requirements for the problems needing attention

in the management of heavy vehicles crossing bridges. Hu B X et al. [7] built a model of the random dense vehicle load of bridge structures and obtained three different degree dense vehicle loads by using the simulated model. Li Y H et al. [8] suggested a method for analyzing the probability of heavy vehicles with adopting the monitored strain data from a structural health monitoring system of a bridge. Tao Fuxian and Du shanpeng [9] introduce the evaluation method and checking calculation points of the bearing capacity of the bridge structure, and give the basis for the carrying capacity of the bridge structure under the overweight load, and introduce several engineering technology and management measures when the overweight vehicles cross the bridge. Wang K and Liu J [10] put forward the safety evaluation conclusion on the basis of bridge status and finite element calculation which ensured the overweight vehicle to cross hollow plate girder bridge safety. Liu Jing and Cao Xintao [11] check the bearing capacity of the bridge, and put forward the corresponding bridge management measures, so as to reduce the harm of overweight vehicles to the highway bridge and improve the bearing capacity of the bridge. W. Han et al. [12] presented a methodology for assessing the safety of pre-stressed concrete box-beam bridges with considering customized transport vehicle load effects. As for large number of bridge collapse accidents due to heavy truck. Zhu Songye et al. [13] suggested a vehicle-bridge coupled vibration model of a rigid-frame bridge for evaluating bridge structure safety under practical traffic loads effects. Evgeny A. Lugovtsev [14] implemented programs with an experimental and analytical method for assessing the technical condition of road bridges for reliability, and revealed the features, conditions of application, positive and negative aspects of each version of the program.

In short, researchers in the word wide still lack data to assist doing safety impact assessment of heavy vehicle load effects for bridge structures. The present study lacks effective support from field measured data. Consequently, by using large amount of strain monitoring data and AN-SYS software, a method is suggested to assess the safety impact of heavy vehicle on the prototype bridge in this paper. Based on large amount of in-situ measured data, the calculated value got by our suggested method is closer to the bridge structure actual situation. We firstly suggested a calculation method for the dynamic reliability calculation of the abnormal load of a type overweight vehicle, and the method can also be extended to do security evaluation for

other abnormal loads. The method is very useful for of the bridge traffic management, and hence can effectively reduce the damage of bridge structures under heavy vehicle load effects.

2. Brief Introduction of the Prototype Bridge

2.1 Structural Health Monitoring System of the Prototype Bridge

The superstructure of the prototype bridge main beam is a continuous box-beam system with a total of eight main piers and 7 main spans. The first span is 145.4 m long and the sixth span is 87 m long, and the 4 center spans are all 144 m long. The cross section of box girder is a single-box and single-chamber. The width of box girder top plate is 12.5 and the base plate width of is 6.8 m. The bridge deck transverse slope is 2.0% and the bridge deck longitudinal slope is 0.15%. The heights of the main beam cross sections change from 8 m to 2.8 m according to 1.6 order power parabola from the supporting base to the mid-span. The thickness of the main beam base plate varies from 1 m to 0.32 m and thickness of the main beam web plate varies 0.9 m to 0.45 m. The main beam is fully prestressed concrete structure with vertical, horizontal and longitudinal prestressed arrangement, and the prestressed tendons are $15\Phi^j15.24\,\text{mm}$ steel strand with the strength: $R_y^b = 1860\,\text{MPa}$, $2\Phi^j12.7\,\text{mm}$ steel strand with the strength: $R_y^b = 1395\,\text{MPa}$ and high strength rebar respectively.

The monitoring points of the SHM in each cross section of the main beam locate near piers, in mid-span and in 1/4 span, with total 20 sections. Among them, there are 8 cantilever end sections, 8 L/4 span sections, and 4 L/2 span sections. The strain variety sensor material object (JMZX-215 type) is shown in Figure 1, which is string type strain gauge. The section locations can be seen in Figure 2. The sensor embedded locations in each section can be seen in Figure 3 with unique given numbers. With the given name of cross section and number, a sensor in the SHMS can be located in the girder uniquely, such as a sensor is named 3-4MID-1, which means that it locates in the top plate center of the mid-span cross-section between pier 3# and pier 4#. The sensors manufacturer is CHANG-SHA KINGMACH HIGHTECHNICS CO., LTD [15]. With the given name of cross section and number, a sensor in the SHMS can be located in the girder uniquely. The sen-

sor measuring time interval is 1 hour. The strain gauge parameters are shown in Table 1. The health monitoring system is still operating normally at present, and a large amount of strain monitored data have been obtained.

Table 1. Parameters of the strain gauge

Name	Range	Sensitivity	Gauge length	Remarks
Intelligent digital vibrating strain gauge	$\pm 1500\ \mu\varepsilon$	$1\ \mu\varepsilon$	157 mm	Strain gauge embedded in concrete

Figure 1. Picture of the JMZX-215 strain gauge
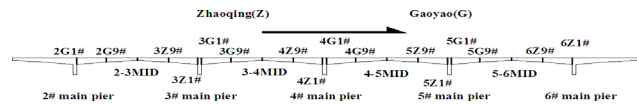
Figure 2. Cross section locations of the embedded sensors of SHMS
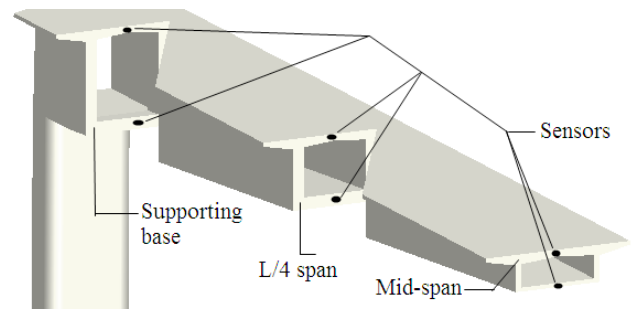
Figure 3. Position of the embedded sensors in half-span of the prototype bridge

2.2 The Acquired Strain Data of the Bridge SHMS

In this article, the data acquired from the sensors 3G1H-1, 3-4MID-1, 4Z9H-1 and 3-4MID-2 are used by us as examples to display the outline of the monitoring data, and the chosen time range is from March 2006 to April 2010. The pre-processed method that how to transform the initial data into strain data can be seen in the papers [16,17]. Figure 4 shows the profile of the original data after several pre-processed steps.
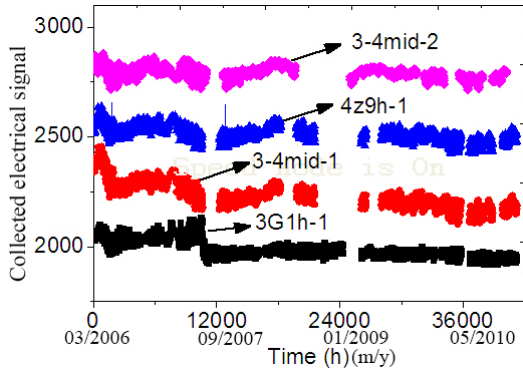
Figure 4. The graph of the monitored data after pre-processed steps

3. Main Idea of Calculation of Initial Quasi Dynamic Reliability

3.1 The Fundamental Theory of First Order Second Moment Method

In this article, the first order second moment method is adopted to calculate structural members' safety index β, and its reliability index β calculation expression can be written as follows:

$$\beta = -\Phi^{-1}(P_f) = (\mu_R - \mu_S)/(\sigma_R^2 + \sigma_S^2)^{1/2} \qquad (1)$$

where Φ^{-1} is the inverse function of the standard normal distribution; μ_R and μ_S are the mean of the resistance and load effects respectively; σ_R and σ_S are the standard deviation of the resistance and load effects respectively. The concrete strength probability distribution function basically obey Gaussian distribution and can be taken as the probability density function of the resistance R.

3.2 The Definition of Quasi Dynamic Reliability

As the concrete compressive and tensile strength parameters are measured by testing machine at a certain strain rate, then, the concrete compressive and tensile strength are called by the name of quasi dynamic compressive strength and quasi dynamic tensile strength. The mean and standard deviation values of the concrete quasi dynamic compressive and tensile strength respectively with 28 days curing are shown in Table 2.

Table 2. The quasi dynamic parameters of concrete compressive and tensile strength used in the prototype bridge

Strength	Mean (units: MPa)	Standard deviation (units: MPa)
compressive	55.12	6.063
tensile	3.2783	0.361

In the meanwhile, as the load effects σ_S (acquired by

SHM) includes the quasi dynamic load effects, such as temperature load effect, vehicle load effects etc., so, we name the safety index the initial quasi dynamic reliability β_q.

3.3 The Calculation of the Initial Quasi Dynamic Reliability β_q

As for the prestress loss and concrete shrinkage and creep etc., the load effects σ_S distribution gradually close to concrete tensile strength distribution with time, therefore, we calculate the initial quasi dynamic reliability β_q by using the quasi dynamic tensile strength distribution as the the resistance σ_R. The method of quasi dynamic load effects σ_S transferred from the monitored data and initial quasi dynamic reliability β_q calculation step both can be seen in the papers [18,19]. Figure 5 illustrates the quasi dynamic load effects σ_S distribution. In the report, the data collected from the sensor 2-3MID-2, which is embedded in the mid-span web plate between the main pier 2# and main pier 3#, are taken as examples, and the selected time range is from March 2006 to October 2006. During March 2006 to October 2006, the bridge has just begun to enter into service, which reflects the quasi dynamic reliability state of the bridge at the beginning of operation. Based on Equation (1), the initial quasi dynamic reliability β_q value is got, seen in Table 3. Since the selected monitored data time range is before the opening of traffic, and so the traffic load effect is not included in the monitored data.
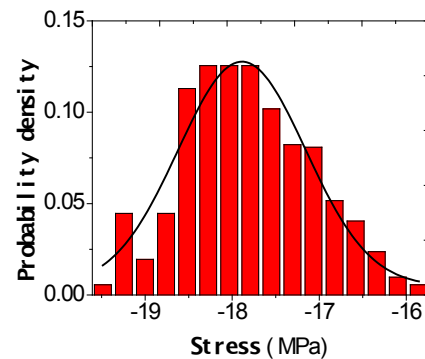
(2-3MID-2) 2006.05 ～ 2006.10

Figure 5. The graph of quasi dynamic load effects σ_S distribution and Gaussian distribution fitting

Table 3. The initial quasi dynamic reliability β_q value in mid-span web plate between main pier#2 and main pier#3

Sensor number	2-3MID-2
The initial quasi dynamic reliability β_q value	10.7903

4. The Building of Simulation Model for Heavy Vehicle Passing through the Bridge

4.1 Building of the FEM Model

In order to obtain the dynamic load effects induced by heavy vehicles, FEM technology is used to simulate heavy vehicles passing through the bridge. Here, the sub-model technology will be used to learn the local responses in the bridge [20,21], which helps to simplify the analysis model and get enough analysis accuracy. A FEM sub-model of the prototype bridge is set up including the girder between the main pier 2# and the main pier 3# (shown in Figure 6). In this model, a 3D element (solid 45 element) with the shortest length 0.25 m is used to simulate concrete, and there are 37,388 elements and 57600 nodes in the sub-mode. The boundary condition of the FEM model is set as consolidation.
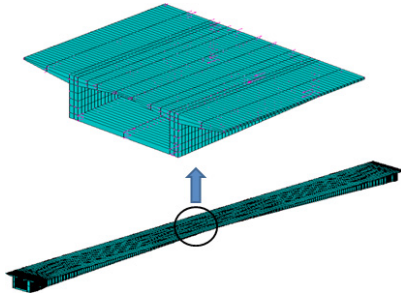
Figure 6. Schematic and mesh mode of FEM sub-model

4.2 Calibration of the Reliability of the Simulation Model

For the sake of checking the reliability of the FEM model, we have done a calibration work on a loading capacity test of the bridge before the bridge came into service. On the test, utmost ten QC-20 main vehicles (a truck loading model with the weight 300 kN defined in a Chinese Specification JTG D60-04 [22]) were used, and they were divided into four loading levels: 900 kN, 1500 kN, 2400 kN, 3000 kN. At present, we have only the static loading test data for the calibration of the FEM model. Figure 7 shows the loading distribution of each loading level, where first loading level included trucks with "①" and second loading level included trucks with "①" and "②", and so on. Figure 8 illustrates the comparison between the measured results and FEM results at the position sensor 2-3MID-2 located, and the two results have a good agreement, and the errors between numerical and tested strains of the four data points shown in Figure 8 are 18.4%, 4.92%, 14.6%, 7.9%, which means that the built FEM model is reliable.

4.3 The Simulation Process

In this paper, the key is to design a reasonable load in FEM model to represent the heavy vehicle. Here we introduce one kind of vehicle loads with four kinds of speeds: A QC-20 heavy truck with about double standard load. The alxe load distribution is shown in Figure 9, and such load will "move" along the span with speed 10 m/s, 20 m/s to learn the response strength around the sensor 2-3MID-2 at the mid-span.

Figure 7. Loading Scheme of the loading capacity test

Figure 8. Comparison between the simulated data and the monitored data (Corresponding to the sensor 2-3MID-2)

Figure 9. Load's distribution of QC-20 heavy vehicle and moving diagram

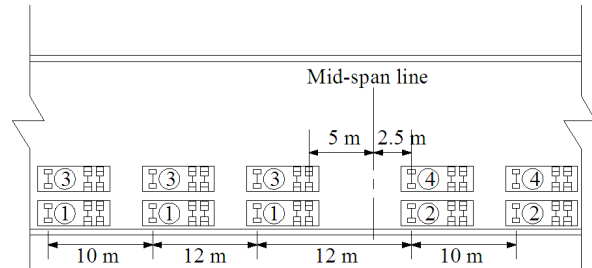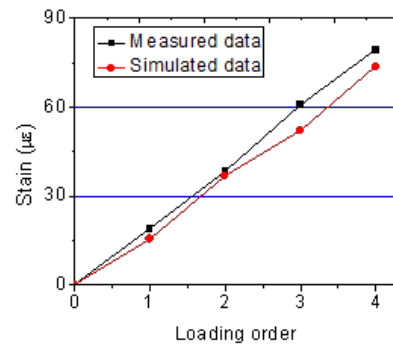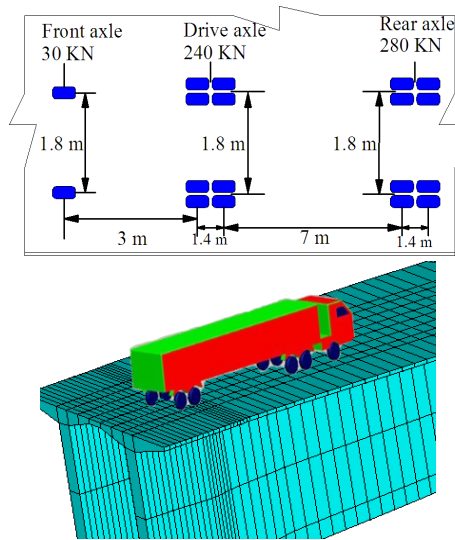Vehicle loads also have impact effect on bridges. Hwang and Nowak [22] developed models for trucks, road surface (roughness) and the bridge, which dealt with the analysis of dynamic loads in bridges, and found that the simulated deflections indicate that the dynamic component is not correlated with the static component, and also found that the dynamic loads are lower for heavier truck and the dynamic loads for two trucks are lower than for single trucks. According to a Chinese Specification JTG D60-04 [23], the impact coefficient of vehicle load takes the value 0.081. By considering the four vehicle loading effects and the dynamic properties, Stress values generated under vehicles passing through the girder in the above case, at the sensor 2-3MID-2 position, can be seen in Figure 10. After we got the stress data, we then do normal distribution statistical analysis, which can be seen from Figure 10, and we can find that the stress data are basically normally distributed. Therefore, we deal with the stress statistical data with Gaussian distribution fitting, seen in Figure 10.
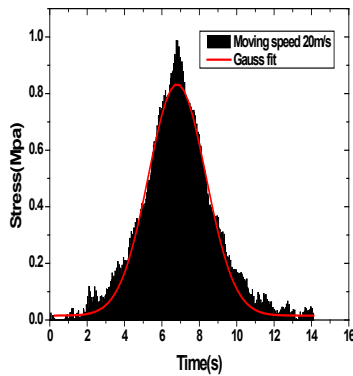

Figure 10. Gaussian distribution fitting of the stress distribution statistics

5. Results and Discussion

5.1 Some Properties of Normal Distribution

The normal distribution has some very important characteristics, such as: if $X \sim N(\mu_X, \sigma_X^2)$ and $Y \sim N(\mu_Y, \sigma_Y^2)$ are statistically independent normal random variables, and also the sum of them satisfies the normal distribution, and can be written as the following formula:

$$X + Y \sim N(\mu_X + \mu_Y, \sigma_X^2 + \sigma_Y^2) \tag{2}$$

5.2 Formula Derivation of Heavy Vehicle Load Effects Impact on Bridge Structure Reliability

According to the stress-strain characteristics of high-strength concrete specified in the standard "code for de-

sign of concrete structures" [24], we assume that the main beam stress state change is in the stage of approximately linear elasticity under heavy vehicle loads impact in this article. Hence, the heavy vehicle load effects and the quasi load effects transformed from the monitored data are statistically independent random variables, through formulas (1) and (2), and the initial quasi dynamic reliability calculation formula with considering the influence of heavy vehicle loads can be derived as follows:

$$\beta_{qc} = \frac{\mu_R - (\mu_M + \mu_{qc})}{\sqrt{\sigma_R^2 + \sigma_M^2 + \sigma_{qc}^2}} \tag{3}$$

where, β_{qc} is the initial quasi dynamic dynamic reliability index considering heavy vehicle effects; μ_R is the mean of the resistance, and μ_M is the mean of quasi load effects transformed from the SHM; σ_R is the standard deviation of the resistance, and σ_M is the standard deviation of the quasi load effects transformed from the SHM; μ_{qc} is the mean of heavy vehicle effects, and σ_{qc} is the standard deviation of the heavy vehicle effects.

By Gaussian distribution fitting of the stress distribution statistics, seen in Figure 10, the values of μ_{qc} and σ_{qc} were obtained, and can been seen in Table 4.

Table 4. The values of μ_{qc} and σ_{qc} corresponding to the sensor 2-3MID-2 embedded in mid-span web plate

Speed	10m/s	20m/s
μ_{qc} (MPa)	0.238	0.238
σ_{qc}^2 (MPa)	0.0797	0.0801

With the data in Table 1 and Table 3, we calculated the dynamic reliability index values β_{qc} with the Equation (3), and then we got the values which are shown in Table 5.

Table 5. The values β_{qc} corresponding to the sensor 2-3MID-2 position embedded in mid-span web plate

Speed	10m/s	20m/s
β_{qc}	10.354	10.640

By comprehensive analysis of the data shown in Table 2 and Table 4, the impact level of heavy vehicle loads on dynamic reliability of the prototype bridge is obtained, and in the paper we name it $\Delta\beta_{qc}$, of which the values can be seen in Table 6.

Table 6. The values $\Delta\beta_{qc}$ caused by heavy vehicle loads

Speed	10m/s	20m/s
$\Delta\beta_{qc}$	0.437	0.151

It can be seen from Figure 9 that the variation range of the stress induced by heavy vehicle is about 1 MPa in the

mid-span web plate of the prototype bridge, and it is in a safe state, because the change range is in the bearing capacity limit and the pressure safety reserve of the concrete materials during the bridge in the early stage of service. According to the above results, under a heavy vehicle intensity influence，the range of variation of the quasi dynamic reliability $\Delta\beta_{qc}$ is about 0.15-0.44 in the mid-span web plate corresponding to the sensor 2-3MID-2 position, of which the meaning is that heavy vehicle load effects have limited impact on bridge safety.

6. Conclusions

As for the difficulties of safety evaluation of load effects of the heavy vehicle for bridges, combine with the large amount of monitored strain data acquired from the SHMS of the prototype bridge and simulation technology, a evaluation method is put forward for assessing the dynamic reliability of this type bridge under heavy vehicle load effects influence in this paper, and the main conclusions are:

1) Assuming that the main beam stress state change is in the stage of approximately linear elasticity under heavy vehicle loads impact, a methodology is presented for the calculation of dynamic reliability of the prototype bridge with considering heavy vehicle load effects, and we found that the heavy vehicle load effects have limited impact on bridge safety. Also, we found that the range of stress change induced by heavy vehicle is small.

2) The statistical analysis of the simulated a type heavy vehicle load effects indicates that they basically obey Gaussian distribution, and hence we can use the first order second moment method to assess the heavy vehicle load effects safety influence on bridge structures.

3) The next research project should pay key attention to the bridge aging, the bridge material strength degradation, shrinkage and creep of concrete etc., and then study the reliability of bridge structures taking into account heavy vehicle load effects. When the prototype bridge served for a long time, conducting the analysis whether the safety reserve of the bridge meets the heavy vehicle load effects safety requirements or not is quite necessary. In the meanwhile, the next step research plan should also focus on finding out the difference between this study's quasi-result and the actual result.

The means suggested in the paper can provide basis and direction for the safety evaluating of bridge structures encountering other abnormal events.

Acknowledgements

Conflict of Interest

There is no conflict of interest.

References

[1] Kirkegaard, P.H., Nielson, S., Enevoldsen, I., 1998. Dynamic vehicle impact for safety assessment of bridges. European Conference on Weigh-in-motion of Road Vehicles.

[2] Zhao, Y., Ren, W., Lv, Y.Zh., 2005. Research on Countermeasures for overweight vehicles crossing bridges. National bridge academic conference of bridge and structural engineering branch of China highway society.

[3] Chang, H., Zhang, Sh.F., Ge, X.K., et al., 2007. Analysis on the harm and prevention of overweight vehicles to highway bridges. Traffic Standardization. (9), 50-52.

[4] Jiang, H., Wei, C., Huang, F., 2009. The Permit Management and Safety Assessment of Shengli Bridge under Overweight Vehicle. IEEE.

[5] Na, H.S., Lee, G.W., Choi, D.H., 2009. Assessment of Vehicle Impact to Edge Beams of U-channel Segmental Concrete Bridges.

[6] Yu, X.F., 2010. Management and reinforcement maintenance measures for overweight vehicles crossing bridges. Northern Transportation. (05), 86-89.

[7] Hu, B.X., Zhang, J.R., Yin, X.F., et al., 2012. Safety Assessment of Bridge Structures under the Random Dense Vehicle Loads. Applied Mechanics & Materials. 117-119, 690-694.

[8] Li, Y.H., Tang, L., Liu, Z., et al., 2012. Statistics and probability analysis of vehicle overloads on a rigid frame bridge from long-term monitored strains. Smart Structures & Systems. 9(3), 287-301.

[9] Tao, F.X., Du, Sh.P., 2013. Structural safety assessment and bridge crossing countermeasures for overweight vehicles. Theoretical research on urban construction (electronic version). (14).

[10] Wang, K., Liu, J., 2014. Safety Evaluation of Structural Behaviors for Overweight Vehicle to Cross Prestressed Concrete Hollow Plate Girder Bridge. Highway Engineering.

[11] Liu, J., Cao, X.T., Fang, Sh.T., 2015. Damage effect of overweight vehicles on highway bridges and bridge crossing management measures. Highway traffic science and Technology (Application Technology Edition). 000(008), 3-5.

[12] Han, W., Yuan, Y., Chen, X., et al., 2018. Safety assessment of continuous beam bridges under heavy-customized transport vehicle load. Journal of Bridge Engineering. 23(6), Article ID 04018030.

[13] Zhu, S.Y., Lu, N.W., Wang, K., et al., 2020. Dynamic Reliability of Continuous Rigid-Frame Bridges under Stochastic Moving Vehicle Loads. Shock and Vibration. 1-13.

[14] Evgeny, A.L., 2021. Justification of the development and application of express assessment programs for road bridges when heavy vehicles pass through them. Structural Mechanics of Engineering Constructions and Buildings. 17(4), 315-323.

[15] Ouyang, Sh., 2009. Control technology of constructing t-rigid frame turret bridge of no.1 bridge for an expressway. Industrial Buildings. Suppl(39), 1079-1065.

[16] Liu, Z., Li, Y.H., Tang, L., et al., 2014. Localized reliability analysis on a large-span rigid frame bridge based on monitored strains from the long-term SHM system. Smart Structures & Systems. 14(2), 209-224.

[17] Li, Y.H., Peng, K.S., Cai, L.R., et al., 2020. Time-varying Reliability Analysis of Long-span Continuous Rigid Frame bridge under Cantilever Construction Stage based on the Monitored Strain Data. Journal of Architectural Environment & Structural Engineering Research. 3(1).

[18] Li, Ying hua et al. Maintenance Management Research of a Large-span Continuous Rigid Frame Bridge Based on Reliability Assessment by Using Strain Monitored Data. Journal of Architectural Environment & Structural Engineering Research, [S.l.], v. 4, n. 2, may 2021.

[19] Ko, J.M., Ni, Y.Q., 2005. Technology developments in structural health monitoring of large-scale bridges. Engineering Structures. 27, 1715-1725.

[20] ANSYS company, 1999. Modeling and Meshing Guide.

[21] Xie, S.M., Jiang, D., Zhao, W.D., 2000. An advanced analysis technique sub-modeling and side-frame example. Journal of Dalian Railway Institute.

[22] Hwang, E.S., Nowak, A.S., 1991. Simulation of dynamic load for bridges. ASCE Journal of Structural Engineering. 117(5), 1413-1434.

[23] The People's Republic of China Ministry of Communications ministerial standard, 2004. General Code for Design of Highway Bridges and Culverts (JTG D60-2004), People Transportation Press, Beijing.

[24] National Standards of the People's Republic of China, 2010. Code for design of concrete structures, GB 50010-2010.

ARTICLE

Effect of Substitution of Cement by Mineral Powders on the Physico-mechanical Properties and Microstructure of Sand Concretes

Belkacem Belhadj[1*] **Justin Houessou**[2] **Nicolas Montrelay**[2] **Michèle Quéneudec**[2]

1. SREML Laboratory, University Amar Telidji, BP 37 G, Laghouat, 03000, Algeria
2. Research unit "EPROAD", University of Picardie Jules Verne, Amiens, 80000, France

ABSTRACT

The approach that contributes to the development of eco-materials in construction is the use of mineral powders, which can improve mechanical properties and reduce cement consumption. This article aims to study the effect of substitution by mass of cement with mineral powders on the physicomechanical properties and microstructure of sand concretes. The used mineral powders are A: the limestone, B: the natural pozzolan, C: the hydraulic lime, D: (1/3 limestone + 1/3 natural pozzolan + 1/3 hydraulic lime), and E: (1/2 natural pozzolan + 1/2 hydraulic lime). The studied percentages are 5%, 10% and 15%, in both separated and combined states. The studied properties are workability, compressive strength, the elasticity modulus in compression, shrinkage and microstructure analysis. The objective is to target the optimal percentage of the substitution of cement with mineral powders, which ensures the best compromise between the main properties of the studied sand concretes. The obtained results show that the optimal percentage is in favor of the substitution of cement by 10% D (1/3 limestone, 1/3 natural pozzolan and 1/3 hydraulic lime). Even the 15% of mineral powder D, presented similar performances compared to the sand concrete (without mineral powders). Finally, in the context of the development of eco-materials, it should be noted that the 10% D and 15% D (1/3 limestone, 1/3 natural pozzolan and 1/3 hydraulic lime) contribute to decrease the use of cement and consequently to reduce of CO_2 emissions.

1. Introduction

Cement manufacturing is an energy-intensive process, about 12%-15% of the total energy consumption of a country [1]. The cement industry has always been among the largest sources of CO_2 emissions [2]. It represents about 7% of total CO_2 emissions worldwide [3]. The CO_2 emission released into the atmosphere is about 900 kg for every ton of cement produced [2], which has a negative effect on the environment. That is why the main requirements of sustainable development in construction are reducing energy consumption, gas emissions, and even the use of water.

*Corresponding Author:
Belkacem Belhadj,
Architecture Department, University Amar Telidji, Laghouat, 03000, Algeria;
Email: b.belhadj@lagh-univ.dz*

Moreover, the use of eco-materials development in construction is an environmentally and sustainable approach that can contribute to lessening the impact of environmental degradation (limiting the greenhouse effect, saving natural resources, health and comfort) [4]. Indeed, it is virtually impossible to imagine a world without concrete. However, we have to improve its environmental impact through the sustainable use of local resources [5].

In this context, the partial substitution of cement for mineral powders can improve the mechanical properties and durability of concretes, while reducing cement consumption, which helps to simply and economically solve some environmental problems [6]. Practically, the use of mineral powders in cementitious composites may present three fields of interest.

The first one is the search for new types of cement [7,8]. Actually, new types of cement, whose mechanical properties meet the needs of cement masonry and architectural engineering, were prepared from ground limestone powder, blast furnace slag, steel slag and gypsum [9]. The second one is the partial substitution of some components of the clinker with other components having hydraulic and/or pozzolanic properties such as, limestone, blast furnace slag and pozzolan for mortar limestone [10,11]. The third one is the partial substitution of artificial Portland cement or Portland cement compound by other mineral powders. In this context, Itim et al. used limestone, pozzolan separated with different percentages [12]; Burgos-Montes et al. substituted a part of cement by limestone, fly ash and silica fume [13]; Dif et al. used combined natural volcanic powders: pozzolan and perlite [14]; Zaitri et al. used dune sand powder and limestone [15,16]; Deepankar used silica fume, and metakaolin [17].

Sand concrete is back in force, due to its specific properties that brought some technical solutions to problems, sometimes, poorly resolved by traditional concrete [18]. Sand concrete is a material intended for the building's structure and architectural elements. It should also be noted that one of the preferred applications of sand concretes in the construction field is the prefabrication of architectural elements, intended to remain apparent, i.e., the various architectural effects, such as shape, finish, color, texture and excellent quality make an essential contribution to the design of façades.

This article aims to study the effect of substitution (by mass) of cement by mineral powders on the physicomechanical properties and microstructure of sand concretes. The used mineral powders are, A: the limestone, B: the natural pozzolan, C: the hydraulic lime, D: (1/3 limestone + 1/3 natural pozzolan + 1/3 hydraulic lime) and E: (1/2 natural pozzolan + 1/2 hydraulic lime). The studied properties are

workability, compressive strength, the elasticity modulus in compression, shrinkage and microstructure analysis. The objective is to target the optimal percentage of the proposed substitution of cement by mineral powders, which ensures the best compromise between the main properties of the studied sand concretes. Furthermore, it reduces the use of cement and thus contributes to the reduction of CO_2 emissions.

2. Materials and Methods

2.1 Materials Used

Both types of sand were used: a local dune sand (DS: 0/63 mm) that covers a very large part of southern Algeria and an alluvial sand (AS: 0/5 mm) that was extracted from the M'zi river crossing the Laghouat region. The sands were used in admixture under a weight ratio determined by correcting the granulometric curve of alluvial sand, in its fine part, by adding dune sand. Bederina et al. studied the mixture of the same sands (alluvial sand and dune sand) and found that the optimum compacity can be obtained with the report AS/DS = 1.7 [19]. Even, Nécira et al. also studied the optimization of a mixture of sands and found that, in the case of alluvial and dune sands, the proportions: (60% of alluvial sand + 40% of dune sand) which are very close to the previous report, seems to be the best combination [20,21]. These types of sand are essentially siliceous [22]. Table 1 includes all their physical properties.

Table 1. Physical characteristics of the used sands.

Characteristics	Dune sand	Alluvial sand	Sand mixture
Apparent density (kg/m^3)	1501	1662	1622
Specific density (kg/m^3)	2587	2425	2485
Fineness modulus	1.98	2.89	2.81
Compactness (%)	0.5754	0.6677	0.6715
Visual Sand Equivalent (%)	90.7	93.5	93.2
Sand Equivalent with piston (%)	81.4	82.2	80.3

For sustainable building solutions, Portland limestone cement type is usually used (of type CPJ-CEM II/A-L 42.5 R). This cement provides similar performances to those obtained with conventional Portland cement. The results of both chemical and physical analyses of the used cement are shown in Tables 2 and 3.

The choice of mineral powders used in this study was inspired from the literature and is essentially based on economic and environmental considerations. These mineral powders are a limestone, which is generally considered as inert filler, a natural pozzolan (active filler) and a hydraulic lime (active filler). The physical properties are mentioned in Table 4.

Table 2. Chemical analysis of the used cement (%).

SiO$_2$	CaO	MgO	Al$_2$O$_3$	Fe$_2$O$_3$	SO$_3$	K$_2$O	Cl	Na$_2$O	Free CaO	Loss	Ins.
16.93	62.23	1.03	5.26	2.82	2.89	0.65	0.02	0.04	1.782	7.83	1.61

Table 3. Physical analysis of the used cement.

Properties	Percentage
Blaine	444.9 (m^2/kg)
Specific density	3030 (kg/m^3)
Apparent density	1032 (kg/m^3)

Table 4. Physical properties of mineral powders.

Physical properties	Limestone	Pozzolan	Lime
Blaine (m^2/kg)	280	388	650
Specific density (kg/m^3)	2700	2850	2750
Apparent density (kg/m^3)	1530	1005	666

The limestone fillers are obtained by wet sieving method (through a sieve of 80 μm) of crushing waste available in a local quarry located on the northern edge of Laghouat city (Algeria). These fillers are intended to supplement the grading curve of the sand in its fine part, which is highly recommended, as fillers, for sand concrete. These fillers contain the following elements: Calcium Carbonate (CaCO$_3$), Silica (SiO$_2$) and Calcium Oxide (CaO) [23].

The natural pozzolan is of volcanic origin. It was extracted from Bouhamidi deposit located south of the city of Beni Saf in Algeria. This is an effusive volcanic rock composition, especially, siliceous Feldspar. This pozzolan is provided as a crushed rock pumice slag type with a grain diameter ranging from 5 mm to10 mm. We first conducted its drying at 105 °C to remove any possible moisture and facilitate its grinding in a Los Angeles-type mill and then sieved it through a sieve of 80 μm. The conservation takes place in a sealed container. The natural pozzolan contains the following elements: aluminum oxide (Al$_2$O$_3$), calcium oxide (CaO), magnesium oxide (MgO) and dioxide sulfur (SO$_2$) [23].

The lime used is a hydraulic lime brought from the Saida plant (SNMC Company - Algeria). It was subjected to sieving through an 80 μm sieve in order to obtain the same size as that of limestone and pozzolan. Hydraulic lime contains the following elements: Calcium Carbonate (CaCO$_3$) and Calcium Hydroxide (Ca(OH)$_2$) [23].

To improve the performance characteristics of the sand concretes, the use of the adjuvant is essential. The used adjuvant is of MEDAPLAST type SP40; it is in accordance with the EN934-2 standard.

2.2 Elaboration of Studied Sand Concretes

The basic composition of the sand concrete (without mineral powders), taken as a reference for our study, is inspired from the work of Belhadj [24]. This composition is shown in Table 5 [24,25]. Let us note that, according to the specifications, the Portland limestone cement contains an initial mineral powder which is the limestone whose proportion ranges from 6% to 20%. Clinker ranges from 80% to 94%. The different mineral powders considered in this study are:

- Mineral powders A: 5%, 10% and 15% of limestone;
- Mineral powders B: 5%, 10% and 15% of natural pozzolan;
- Mineral powders C: 5%, 10% and 15% of hydraulic lime;
- Mineral powders D: 5%, 10% and 15% of (1/3 limestone + 1/3 natural pozzolan + 1/3 hydraulic lime);
- Mineral powders E: 5%, 10% and 15% of (1/2 natural pozzolan + 1/2 hydraulic lime).

The different percentages of substitution used are 5%, 10% and 15% for each type of mineral powder: A, B, C, D and E. The mineral powders are substituted for cement in mass percentages. The water / (cement + % powders) is set to 0.6 for all compositions tested (Table 5). This value, corresponding to a slump of 9 cm with the Abrams cone, ensures good workability for the basic composition of sand concrete (without mineral powders) made with Portland limestone cement.

To better homogenize the mixture, which contributes to a better quality of sand concrete and therefore the proper control of the various properties of the finished product, the following procedure was adopted. First a dry mixing of cement and mineral powders for one minute at low speed was made [26]. Then, the alluvial-sand dune and limestone fillers are added, in a dry mixture performed for three minutes at a low speed [22,26]. Finally, the mixing water is added gradually to the mixture without breaking the kneading in order to ensure the good homogenization of the mixture for three other minutes at a low speed [22,26].

Table 5. The studied compositions of the sand concretes.

Composition	A	B	C	D	E
Cement (kg/m^3)	297.5: 85% 315.0: 90% 332.5: 95% 350.0: 100%	297.5: 85% 315.0: 90% 332.5: 95% 350.0: 100%	297.5: 85% 315.0: 90% 332.5: 95% 350.0:100%	297.5: 85% 315.0: 90% 332.5: 95% 350.0: 100%	297.5: 85% 315.0: 90% 332.5: 95% 350.0: 100%
Limestone powder (kg/m^3)	52.5: 15% 35.0: 10% 17.5: 5% 00.0: 0%	- - - -	- - - -	17.5: (1/3)15% 10.83: (1/3)10% 5.83: (1/3)5% -	00.0 00.0 00.0 00.0
Pozzolan powder (kg/m^3)	- - - -	52.5: 15% 35.0: 10% 17.5: 5% 00.0: 0%	- - - -	17.5: (1/3)15% 10.83: (1/3)10% 5.83: (1/3)5% -	26.25:(1/2)15% 17.5:(1/2)10% 8.75:(1/2)5% -
Lime powder (kg/m^3)	- - - -	- - - -	52.5: 15% 35.0: 10% 17.5: 5% 00.0: 0%	17.5: (1/3)15% 10.83: (1/3)10% 5.83: (1/3)5% -	26.25: (1/2)15% 17.5: (1/2)10% 8.75:(1/2)5% -
(DS) + (AS) Dune Sand + alluvial Sand (kg/m^3)	1316				
Limestone filler (kg/m^3)	135				
Water (l/m^3)	210				
Superplasticizer (%) (based on the weight of cement)	2				

After mixing, the material is poured into molds: (40 × 40 × 160 mm^3) for the shrinkage tests and (70 × 70 × 280 mm^3) for the mechanical tests. The specimens are demoulded after 24 hours and the samples are kept, until the day of the test, in the same room, where the indoor climatic conditions of the laboratory room are closer to the weather conditions, namely at a temperature of (20 °C ± 5 °C), and relative humidity of (50% ± 10%).

2.3 Experimental Techniques

The study of the consistency of the sand concrete was made by the slump test with the Abrams cone according to the NF P18-451 standard. The compressive strength was determined using a universal press of type "Controls", in accordance with the standard (EN196-1). The compression test was performed on cubes of (70 × 70 mm^2). The modulus of elasticity in compression was determined by a Shimadzu type press at a ramp rate equal to 500 N/s, in accordance with the standard NBN EN 1015-11.

The shrinkage was measured using an instrument of a controls type prismatic sample (40 × 40 × 160 mm^3). This instrument is equipped with a comparator for performing measurements with an accuracy of less or equal to 0.005 mm; the test is described by the standard (NF P 15-433) [27].

Infrared analysis was carried out by a Shimadzu IR spectrometry Prestige-2. This technique is very interesting and allows the identification of functional groups from their vibrational properties within a cementitious material after hydration. Infrared radiation excites vibration modes (bond stretching or bending) that characterize the chemical bonds and the different species coexisting in the hydrated products after adding minerals. The analyzed samples were previously ground and mixed with potassium bromide (KBr) at 2 mg of sample to 190 mg of KBr. The whole mixture is placed in a cylindrical mold between two metal pads and then subjected to a pressure of 8 tons in a press with a piston and a pump. The obtained pellets were analyzed by transmission.

The X-ray analysis by diffraction was performed using a PHILIPS X'Pert diffractometer type on samples of concrete, ground and screened to an 80 µm screen.

3. Results

The interpretation of results focuses, first of all, on the study of the effect of the substitution of cement by mineral powders on the physicomechanical properties of the studied sand concretes, i.e., workability, compressive strength and shrinkage. Then, on their microstructure, let us note that the study of the influence of mineral powders on the microstructure was limited to only the sand concrete con-

taining the mineral powder D.

3.1 Workability

Figure 1 shows the effect of mineral powders on the workability of the studied concretes. When the percentage of the mineral powder A increases in the cement, the workability of the studied sand concrete begins to increase starting from a mineral powder proportion equal to 10%. The consistency of sand concrete is highly plastic for mineral powder proportions of 10% and 15%. This increase in workability can be explained by the weak Blaine surface of the limestone filler (280 m^2/kg) compared to that of the cement (444.9 m^2/kg). Indeed, other parameters can also affect the workability like the form of the filler grains, the ration water/bender, etc.
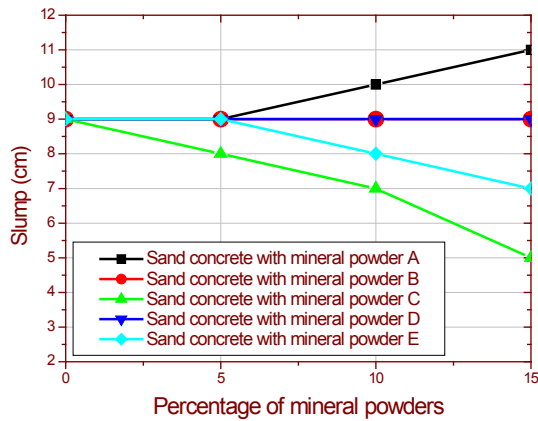

Figure 1. Workability of the studied sand concretes.

When the mineral powders percentage of B or D, increases in cement, the workability of the compositions tested is almost similar to that of the basic composition of sand concrete (without mineral powders), with a slump value of 9 cm. In the case of mineral powder B, this can be explained by the Blaine surface of pozzolan (388 m^2/kg) which is barely less than that of the cement (444.9 m^2/kg). In the case of mineral powder D, this can be explained by the Blaine surface of the powder (439.33 m^2/kg) which is very close to that of the cement. Let us note that the Blaine surface of the mineral powder D is taken as the average of the three fillers (limestone, pozzolan and lime).

When the percentage of the mineral powders C and E increases in the cement, the workability of the corresponding sand concretes decreases between 5% and 15% of mineral powders. Let us note that the composition containing the mineral powder C (lime approximate) gave the lowest slump values compared to the other mineral powders (slump value ≤ 4 cm). The lowest value was re-

corded with 15% of mineral powder C. This weak workability may be explained by the Blaine surface of the lime (650 m^2/kg) which is higher than that of the cement, for different powder percentages. With mineral powder E, the workability also decreases, but in this case this can be explained by the presence of pozzolan in the mineral powder.

Finally, it should be noted that, as far as workability, mineral powders B and D seem to be the most interesting.

3.2 Compressive Strength

The compressive strength generally projects an overall picture of the quality of concrete; it is the key element in the design of concrete structures. According to Figure 2, all the studied sand concretes containing 5% of mineral powders gave compressive strength values greater than that of the basic composition of sand concrete (without mineral powders), except in the case of mineral powder A. The optimum mineral powder percentages of A and C are very close to those of the literature for mortars which are 4% and 5% respectively [12,13], but for the mineral powder percentage of B is about 10% to 20% [12]. On the other hand, the results of the compressive strength of the sand concrete for the different percentages of lime are slightly better compared to mortars with cement-lime at 28 days, which the experimental campaign ranges from 0.4 MPa to 13 MPa [28], but significantly better at 90 days.
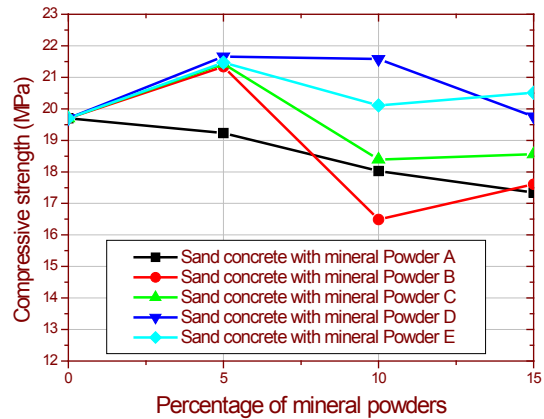

Figure 2. Compressive strength of studied sand concretes at 90 days.

According to Figure 2, all the sand concretes studied with 5% mineral powders gave compressive strength values greater than those of the sand concretes with 10% and 15%. The mineral powder D is better for a mineral powder percentage of 5%, 10% and 15%. The compressive strength of the composition containing 15% of mineral

powder E is slightly higher than that of the composition containing 15% of mineral powder D. Therefore, we can opt for the mineral powder D values since, with this powder, the consistency of the sand concrete is more interesting.

Figure 3 shows, for the four types of selected sand concretes, the compressive strength recorded at 28 days and at 90 days. A higher percentage of mineral powder D (15%) increases the difference in compressive strength between 28 days and 90 days.
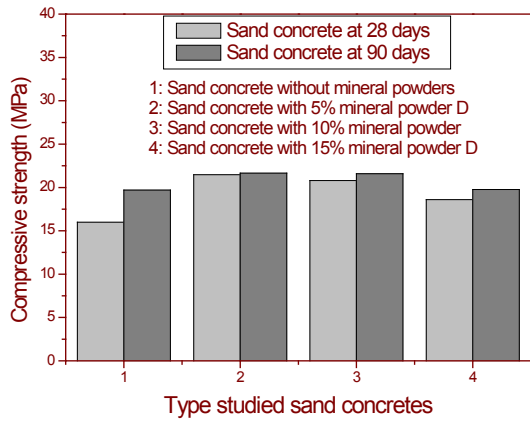

Figure 3. Compressive strength of studied sand concretes with mineral powders D.

Generally, there is always a relationship between compressive strength and density, in the case of building materials [29]. For this study, a relationship between the compressive strength at 28 days and the density has been found; the latter follows a polynomial equation of type:

$Y = a + b.x + c.x^2$ with a correlation coefficient $R^2 = 0.711$ as shown in Figure 4. Where "Y" represents the compressive strength and "x" represents the density. In summary, mineral powder D has an interest in compressive strength compared to the other types of mineral powders, more particularly the composition containing 10% of mineral powder D. It should also be noted that even the composition containing 15% of mineral powder D has a compressive strength similar to that of the basic composition of sand concrete (without mineral powders).

3.3 Elasticity Modulus in Compression

The tests of the elasticity modulus in compression are made for two compositions of sand concretes, namely the basic composition (without mineral powders) and the composition of sand concrete with 10% of mineral powders D (optimal percentage of the substitution of cement by mineral powders). These tests were carried out on prisms having a section (40×40 mm^2). The results of the elasticity modulus in compression are mentioned in Table 6. The elasticity modulus in compression for the sand concrete with 10% of mineral powders D was improved by about + 8.35% compared to the basic composition of sand concrete (without mineral powders).
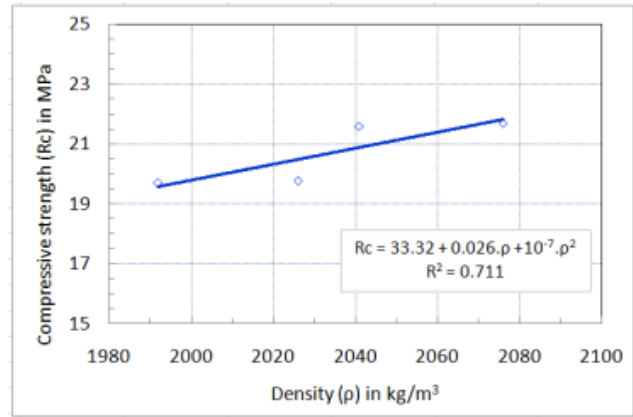

Figure 4. Relationship between the compressive strength at 28 days and the density.

Table 6. Elasticity modulus in compression.

Sand concrete type	Elasticity modulus in compression (MPa)	Contrainte maximale (MPa)
Sand concrete: without mineral powders	387.36	5.63615
Sand concrete: with 10% mineral powders D	419.73	5.63679

The study shows the displacement as a function of the maximum compressive stress in the elastic part of the studied concretes. For a maximum compressive stress of 5.63615 MPa in the elastic zone, it was recorded a displacement of 0.94862 mm for the composition of sand concrete without mineral powders as shown in Figure 5. Nevertheless, for a maximum compressive strength of 5.63679 MPa in the elastic zone, it was recorded a displacement of 0.86408 mm for the composition of the sand concrete with 10% of mineral powder D as shown in Figure 6. The variation of the displacement with respect to the compressive strength shows the advantage of the composition with 10% of powder D, compared to the composition of sand concrete (without mineral powders), with a reduction of 0.08454 mm (i.e. − 8.91%). For example, Figure 5 and Figure 6 show the results of the elastic modulus in compression test which shows the maximum compressive stress in the elastic part.
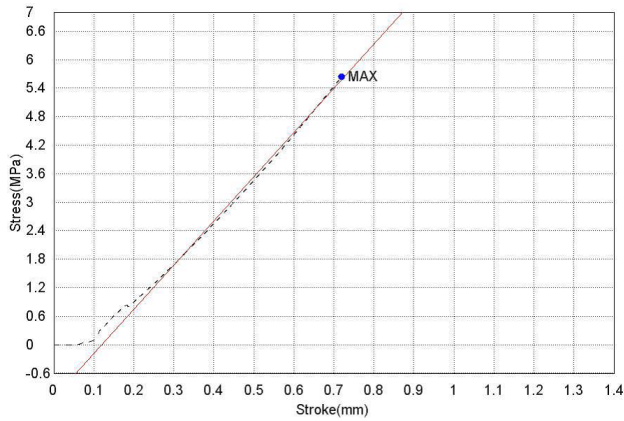
Figure 5. Displacement versus maximum compressive stress (sand concrete without mineral powders).

3.4 Choice of Optimal Percentage

In order to choose the optimal percentage, the best three percentages, i.e., 5%, 10% and 15% of mineral powder D, were selected. These three percentages presented the best compromise between the studied properties, whose values are shown in Table 7. In order to deepen the study of these compositions, tests of shrinkage have been made. Figure 7 shows the development of their shrinkage as a function of age (between 0 and 28 days). It is clear that the sand concretes with mineral powder D present higher shrinkage at 28 days compared to the sand concrete

without powders. The shrinkage tends to stabilize after 21 days. This increase in shrinkage is in agreement with that observed by Itim et al. [12].
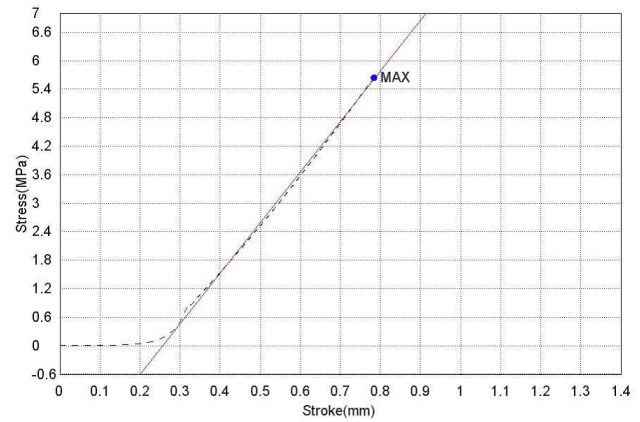

Figure 6. Displacement versus maximum compressive stress (sand concrete with mineral powders).

In these three compositions, it was found that the optimum composition that constitutes the best compromise between the properties studied, i.e., workability, compressive strength and shrinkage, is that containing 5% of mineral powder D. The composition of sand concrete containing 10% of mineral powder D is approaching that 5% of mineral powder D. So for economic and environmental considerations, we opt for the formulation of 10% D.

Table 7. Physico-mechanical properties and shrinkage of the studied sand concretes.

| Studied sand concrete Type	Density (kg/m³)	Compressive strength at 90 days (MPa)	Shrinkage at 90 days (mm/m)
Sand concrete without mineral powders. Improvement (%)	1992.57 ± 11.32	19.70 ± 0.55 00%	0.529 ± 0.022 00%
Sand concrete with 05% mineral powder D (limestone + pozzolan + lime). Improvement (%)	2076.98 ± 22.91	21.66 ± 0.30 + 9.94%	0.681 ± 0.020 + 28.73%
Sand concrete with 10% mineral powder D (limestone + pozzolan + lime). Improvement (%)	2041.53 ± 19.36	21.58 ± 0.23 + 9.54%	0.720 ± 0.034 + 36.10%
Sand concrete with 15% mineral powder D (limestone + pozzolan + lime). Improvement (%)	2026.29 ± 15.51	19.76 ± 0.66 - 0.30%	0.685 ± 0.033 + 29.48%
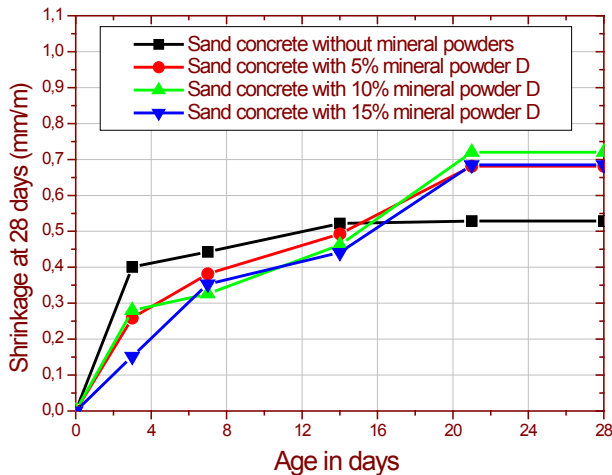
Figure 7. Shrinkage of studied sand concretes at 28 days.

3.5 Microstructure Analysis

3.5.1 Infrared Spectrometric Analysis in Fourier Transform (FTIR)

The spectrum obtained after the analysis of Sample 1 (without mineral powders) and Sample 2 (with 10% of mineral powder D) is shown in Figure 8. The reduced peak at 3641 cm^{-1} in sample 1 is due to the O-H stretching vibration of portlandite [30,31]. The disappeared calcium hydroxide reacted with the siliceous and aluminous compounds and those of pozzolan cement to form hydrated calcium silicates and aluminates. First, C-S-H hydrate (calcium silicate hydrate), resulting from the dominant C_3S component, is responsible for most of the mechanical properties of the cured material due to its binding power. Many bands of the Si-O-Si (918 cm^{-1}, 925 cm^{-1}, 935 cm^{-1}) anhydrous C_3S don't show the formation of calcium silicate hydrates. This hydrate is spotted, on the one hand to 1005 cm^{-1} which explains the change in the environment of the chemical bond of Si-O (C_3S that hydrates in C-S-H) [30], and secondly by the O-H stretching vibration of bonds water molecules constituting the hydrated phase C-S-H 3450 cm^{-1} [32]. The calcium silicate hydrates (C-S-H) are the main bond phases for several concretes [33]. Calcium silicate hydrate (C-S-H), the most important Portland cement hydration product, determines the mechanical properties and durability of cementitious materials [34].

We also observed bands located in 711 cm^{-1}, 873 cm^{-1}, 2513 cm^{-1}, 1797 cm^{-1}, 2875 cm^{-1} and 2983 cm^{-1} which correspond to the C-O group of calcite in the two samples (1 and 2). Indeed, in sample 2, the reduced band intensi-

ties at 711 cm^{-1} and 873 cm^{-1} [35], correspond to the calcite and suggest that calcite participates in hydration reactions in the presence of calcium aluminates to form hydrated calcium carboaluminates. Also, between 1006 cm^{-1} and 1200 cm^{-1}, we have a mixture of hydrated aluminates: C_4AH_{13} of 1083 cm^{-1} and C_3AH_6 of 1150 cm^{-1}.

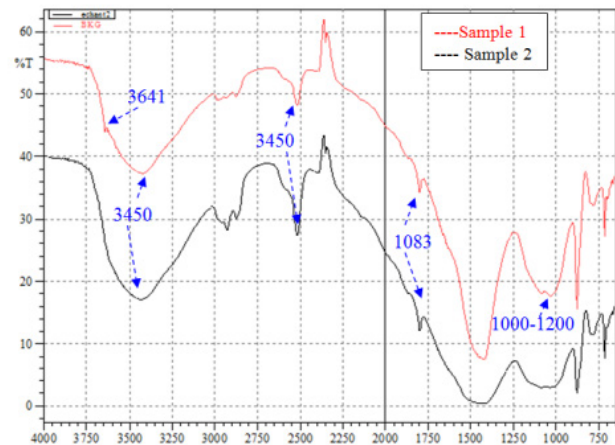**Figure 8.** Spectrum of the studied sand concretes—Sample 1: without mineral powders and Sample 2: with 10% mineral powder D.

C_3AH_6 is a phase much more stable and is obtained by changing intermediate phases such as C_4AH_{13} phase, according to the conditions and environment of hydration of C_3A. The coexistence of these very stable phases with other silicate phases contributes to the improvement of the mechanical properties of sample 2 (sand concrete with 10% of mineral powders D), contrary to sample 1 (sand concrete without mineral powders).

3.5.2 X-ray Chemical Analysis by Diffraction

According to the diffractogram of the sand concrete without mineral powders (Figure 9) and the diffractogram of sand concrete with 10% mineral powders D (Figure 10), it was found that the concrete with mineral powders led to the development of calcium silicate hydrates (C-S-H) and hence improved the mechanical properties of the material. This is explained by:

1) The increase in the intensity of the quartz of about 1500 to 3000, can be explained by the presence of natural pozzolan which is rich in silica.

2) The decrease in the intensity of the calcite of about 1500-800.

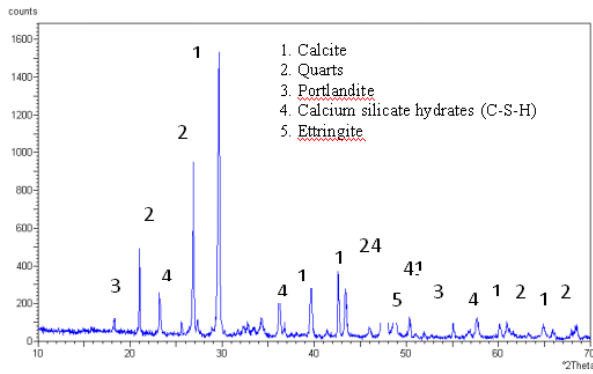3) The decrease in the intensity of portlandite, because of the probable presence of hydraulic lime.

Figure 9. X-ray diffractogram analysis of the sand concrete without mineral powders.
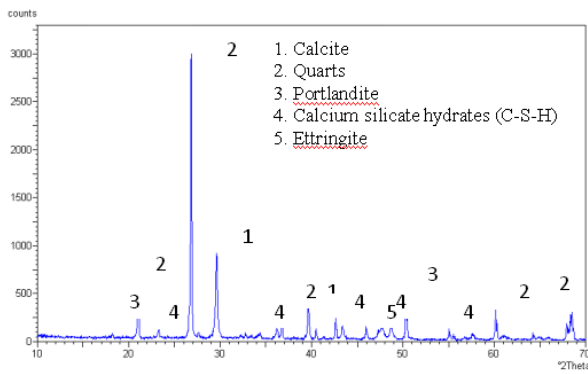

Figure 10. X-ray diffractogram analysis of the sand concrete with mineral powders.

4. Discussion

The advantage of the results of the compressive strength at 28 days and at 90 days is in favor of the sand concretes with mineral powder (D) for 5%, 10% and 15% compared to the sand concretes with 5%, 10% and 15% of the mineral powders (A, B and C) used separated. This observation confirms the advantage of several types of research on the use of both mineral powders [14-16,36], and the use of three mineral powders [10,37]. For example, the test results showed that the addition of limestone filler, blast furnace slag, and natural pozzolan, incorporated simultaneously in cement improves the mechanical behavior of limestone mortars [37].

Furthermore, from the results of the effect of mineral powders on the physicomechanical properties and the microstructure analysis, we can conclude that the use of 10% of powder D has an advantageous effect on the development of the chemical reactions of the sand concrete, which are confirmed by the cross interpretation of the results relating to the Fourier transform infrared spectrometry (FTIR) analysis and the analysis by X-ray diffraction.

These two techniques have shown the development of calcium silicate hydrates (C-S-H). Moreover the coexistence of these very stable phases with the other silicate phases, contributes to the improvement of the mechanical properties of sand concrete with 10% of mineral powder D, contrary to sand concrete without mineral powders.

Finally, the advantage of this approach is for environmental considerations: reduction of the use of cement and significantly reduced CO_2 emissions, and technical considerations: improvement of the mechanical performance and durability of the studied concretes or mortars.

5. Conclusions

In order to study the effect of substitution (by mass) of cement by mineral powders on the physicomechanical properties and microstructure of sand concretes, different mineral powders have been studied, such as A: the limestone, B: the natural pozzolan, C: the hydraulic lime, D: (1/3 limestone + 1/3 pozzolan + 1/3 lime) and E: (1/2 pozzolan + 1/2 lime), with 5%, 10% and 15%, in both separated and combined states. Considering the obtained results, the following conclusions can be drawn:

• The mineral powder D is better for a mineral powder of 5%, 10% and 15% compared to other mineral powders.

• The composition of sand concrete containing 10% of mineral powder D is approaching 5% of mineral powder D. So for economic and environmental considerations, we opt for the formulation of 10% mineral powder D.

• The 15% of mineral powder D presented similar performances compared to the sand concrete (without mineral powders).

• The elasticity modulus in compression for the sand concrete with 10% of mineral powders D was improved by about + 8.35% compared to the sand concrete (without mineral powders).

• The Microstructure analysis showed the coexistence of very stable phases with other silicate phases contributes to the improvement of the mechanical properties of sand concrete with 10% of mineral powders D compared to sand concrete without mineral powders.

• In the economical and environmental aspect, the powder D (limestone, natural pozzolan and hydraulic lime), gave the optimal percentage, especially with the proportion of 10%, which can help to reduce CO_2 emissions and therefore against global warming.

• In the technical aspect, the microstructure study showed the beneficial effect of 10% mineral powders D compared to the sand concrete without mineral powders on the development of hydration reactions, leading thus to the improvement of its mechanical strength.

• Its mechanical properties allow it to be considered

a good eco-material development in construction, which can be used in both structural elements and architectural elements.

Author Contributions

Author 1 > Belkacem BELHADJ, University of Amat Tledji, Laghouat, Algeria:

- The presented work falls within the framework of my research works.

- Corresponding author.

Author 2 > Justin HOUESSOU, Research unit "EPROAD", University of Picardie Jules Verne, Amiens, France:

- A researcher who has significantly contributed in the Infrared spectrometry analysis Fourier transform (FTIR) tests.

Author 3 > Nicolas MONTRELAY, Research unit "EPROAD", University of Picardie Jules Verne, Amiens, France:

- A researcher who has significantly contributed in the elasticity modulus in compression tests.

Author 4 > Michèle QUÉNEUDEC, Research unit "EPROAD", University of Picardie Jules Verne, Amiens, France:

- A researcher teacher who has significantly contributed in the methodology and wording the paper.

Conflict of Interest

No Conflict of Interest in Online Web System and Offline.

Funding

References

[1] Madlool, N.A., Saidur, R., Hassain, M.S., et al., 2011. A critical review on energy use and savings in the cement industries. Renewable and Sustainable Energy Reviews. 15, 2042-2060.
DOI: https://doi.org/10.1016/j.rser.2011.01.005

[2] Benhelal, E., Zahedi, G., Shamsaei, E., et al., 2013. Global strategies and potentials to curb CO_2 emissions in cement. Journal of Cleaner Production. 51, 142-161.
DOI: https://doi.org/10.1016/j.jclepro.2012.10.049

[3] Ali, M.B., Saidur, R., Hossain, M.S., 2011. A Review on emission analysis in cement industries. Renewable and Sustainable Energy Reviews. 15, 2252-2261.
DOI: https://doi.org/10.1016/j.rser.2011.02.014

[4] Escadeillas, G. (editor), 2006. Ecomaterials in construction: Challenges and prospects. Seventh Edition of the Scientific Meetings of the Group Francophone for Research and Training on Concrete (RF)^{2}B; 2006 Jun 19-20; Toulouse, France.

[5] Flatt, R.J., Roussel, N., Cheeseman, C.R., 2012. Concrete: An ecomaterial that needs to be improved. Journal of the European Ceramic Society. 11, 2787-2798.
DOI: https://doi.org/10.1016/j.jeurceramsoc.2011.11.012

[6] Oliveira, L.A.P., Jalali, S., Fernandes, J.M., et al., 2005. The use of metakaolin in the production of environmentally efficient concrete. Materials and Structures. 38, 403-410.
DOI: https://doi.org/10.1007/BF02479308

[7] Lin, Y., Zhou, S., Li, F., et al., 2012. Utilization of municipal sewage sludge as additives for the production of eco-cement. Journal of Hazardous Materials. 213-214, 457-465.
DOI: https://doi.org/10.1016/j.jhazmat.2012.02.020

[8] Weiguo, S., Mingkai, Z., Qinglin, Z., 2006. A New kind of eco-cement made of cement klin dust and granular blast furnace slag. Journal of Wuhan University of Technology—Materials Science Edition. 21 N° 1, 143-146.
DOI: https://doi.org/10.1007/BF02861493

[9] Zongshou, L., Qian, Z., 2009. Strength of limestone-based non-calcined cement and its properties. Journal of Wuhan University of Technology—Materials Science Edition. 471-475.
DOI: https://doi.org/10.1007/s11595-009-3471-8

[10] Makhloufi, Z., Kadri, E.H., Bouhicha, M., et al., 2012. Resistance of limestone mortars with quaternary binders to sulfuric acid solution. Construction and Building Materials. 26, 497-504.
DOI: https://doi.org/10.1016/j.conbuildmat.2011.06.050

[11] Makhloufi, Z., Kadri, E.H., Bouhicha, M., et al., 2012. The strength of limestone mortars with quaternary binders: Leaching effect by demineralised water. Construction and Building Materials. 36, 171-181.
DOI: https://doi.org/10.1016/j.conbuildmat.2012.04.112

[12] Itim, A., Ezziane, K., Kadri, E.H., 2011. Compressive strength and shrinkage of mortar containing various amounts of mineral additions. Construction and Building Materials. 25, 3603-3609.
DOI: https://doi.org/10.1016/j.conbuildmat.2011.03.055

[13] Burgos-Montes, O., Palacios, M., Rivilla, P., et al., 2012. Compatibility between superplasticier admixtures and cements with mineral additions. Construction and Building Materials. 31, 300-309.
DOI: https://doi.org/10.1016/j.conbuildmat.2011.12.092

[14] Dif, F., Douara, T.H., Zaitri, R., et al., 2020. Effects of combined natural volcanic powders on the thermo-physical and mechanical properties of structural eco-concrete. Journal of Building Engineering. 32, 101835.
DOI: https://doi.org/10.1016/j.jobe.2020.101835

[15] Zaitri, R., Bederina, M., Bouziani, T., et al., 2014. Development of high performances concrete based on the addition of grinded dune sand and limestone rock using the mixture design modelling approach. Construction and Building Materials. 60, 8-16.
DOI: https://doi.org/10.1016/j.conbuildmat.2014.02.062

[16] Zaitri, R., Guettala, S., Bederina, M., 2018. Physico-mechanical properties of mortars based on the addition of dune sand powder and the recycled fines using the mixture design modelling approach. Journal of Adhesion Science and Technology. 32(15), 1613-1628.
DOI: https://doi.org/10.1080/01694243.2018.1434032

[17] Ashish, D.K., 2019. Concrete made with waste marble powder and supplementary cementitious material for sustainable development. Journal of Cleaner Production. 211, 716-729.
DOI: https://doi.org/10.1016/j.jclepro.2018.11.245

[18] Baron, J., 1994. Sand concrete characteristics and use practices. Press of the National School of Bridges and Shod: Auckland.

[19] Bederina, M., Khenfer, M.M., Dheilly, R.M., et al., 2005. Reuse of local sand: Effect of limestone filler proportion on the rheological and mechanical properties of different sand concrete. Cement and Concrete Research. 35, 1172-1179.
DOI: https://doi.org/10.1016/j.cemconres.2004.07.006

[20] Nécira, B., Guettala, A., Guettala, S., 2017. Study of the combined effect of different types of sand on the characteristics of high performance self-compacting concrete. Journal of Adhesion Science and Technology. 31, 1912-1928.
DOI: https://doi.org/10.1080/01694243.2017.1289829

[21] Douara, T.H., Guettala, S., 2019. Effects of curing regimes on the physico-mechanical properties of self-compacting concrete made with ternary sands. Construction and Building Materials. 195, 41-51.
DOI: https://doi.org/10.1016/j.conbuildmat.2018.11.043

[22] Bederina, M., Gotteicha, M., Belhadj, B., et al., 2012. Drying shrinkage studies of wood sand concrete—Effect of different wood treatments. Construction and Building Materials. 36, 1066-1075.
DOI: http://dx.doi.org/10.1016/j.conbuildmat.2012.06.010

[23] Belhadj, B., 2016. Contribution to the valorisation of local materials and waste to the formulation of insulating-carrier lightweight sand concretes intended for the construction in arid environments (Case of Laghouat city) [PhD thesis]. Laghouat: University of Laghouat, Algeria.

[24] Belhadj, B., 2007. Improved thermo-physical properties of sand concretes lightened by wood shavings in arid environments (Case of the Laghouat city) [Master's thesis]. Laghouat: University of Laghouat.

[25] Belhadj, B., Bederina, M., Benguettache, K., et al., 2014. Effect of the type of sand on the fracture and mechanical properties of sand concrete. Advances in Concrete Construction. 2, 13-27.
DOI: http://dx.doi.org/10.12989/acc2014.2.1.013

[26] Bederina, M., Marmoret, L., Mezreb, K., et al., 2007. Effect of the addition of wood shavings on thermal conductivity of sand concretes: Experimental study and modelling. Construction and Building Materials. 21, 662-668.
DOI: https://doi.org/10.1016/j.conbuildmat.2005.12.008

[27] Dupain, R., Lanchan, R., Saint-Arroman, J.C., 1995. Aggregates, soils, cement and concretes. Edition Casteilla: France.

[28] Ramesh, M., Azenha, M., Lourenço, P.B., 2019. Quantification of impact of lime on mechanical behaviour of lime cement blended mortars for bedding joints in masonry systems. Construction and Building Materials. 229, 116884.
DOI: https://doi.org/10.1016/j.conbuildmat.2019.116884

[29] Neville, A.M., 2000. Concrete properties, Edition Eyrolles: France.

[30] Horgnies, M., Willieme, P., Gabet, O., 2011. Influence of the surface properties of concrete on the adhesion of coating: Characterization of the interface by peel test and FT-IR spectroscopy. Progress in Organic Coatings. 72, 360-379.
DOI: https://doi.org/10.1016/j.porgcoat.2011.05.009

[31] Ahmari, S., Ren, X., Toufigh, V., et al., 2012. Production of geopolymeric binder from blended waste concrete powder and fly ash. Construction and Building Materials. 35, 718-729.
DOI: https://doi.org/10.1016/j.conbuildmat.2012.04.044

[32] Nozahic, V., Amziane, S., 2012. Influence of sunflower aggregates surface treatments on physical properties and adhesion with a mineral binder. Composites: Part A. 43, 1837-1849.
DOI: https://doi.org/10.1016/j.compositesa.2012.07.011

[33] Ebbert, C., Grundmeier, G., Buitkamp, N., et al., 2014. Toward a microscopic understanding of the calcium-silicate-hydrates/water interface. Applied Surface Science. 290, 207-214.
DOI: https://doi.org/10.1016/j.apsusc.2013.11.045

[34] Liu, X., Feng, P., Li, W., et al., 2021. Effects of pH on the nano/micro structure of calcium silicate hydrate (C-S-H) under sulfate attack. Cement and Concrete Research. 140, 106306.
DOI: https://doi.org/10.1016/j.cemconres.2020.106306

[35] Zhang, D.J., Zhao, J.H., Wang, D.M., et al., 2018. Comparative study on the properties of three hydraulic lime mortar systems: Natural hydraulic lime mortar, cement-aerial lime-based mortar and slag-aerial lime-based mortar. Construction and Building Materials. 186, 42-52.

DOI: https://doi.org/10.1016/j.conbuildmat.2018.07.053

[36] Szostak, B., Golewski, G.L., 2021. Rheology of cement pastes with siliceous fly ash and the CSH nano-admixture. Materials. 14, 3640.
DOI: https://doi.org/10.3390/ma14133640

[37] Makhloufi, Z., Bouziani, T., Hadjoudja, M., et al., 2014. Durability of limestone mortars based on quaternary binders subjected to sulfuric acid using drying-immersion cycles. Construction and Building Materials. 71, 579-588.
DOI: http://dx.doi.org/10.1016/j.conbuildmat.2014.08.086

EDITORIAL

Construction Technology of Pipe Jacking Method through Underground Obstacles

Jianyong Han[1,3]   Dongfeng Jia[2]   Fushun Yan[2]   Yue Zhao[4*]   Dong Liu[1]   Qinghai Wang[1]

1. School of Civil Engineering, Shandong Jianzhu University, Jinan, Shandong, 250101, China
2. The Third Construction Co.,Ltd. of CTCE Group, Tianjin, 300163, China
3. Key Laboratory of Building Structural Retrofitting and Underground Space Engineering (Shandong Jianzhu University), Ministry of Education, Jinan, Shandong, 250101, China
4. Science and Technology Service Platform, Qilu University of Technology (Shandong Academy of Sciences), Jinan, Shandong 250000, China

---

Due to the increase in the global urban population and the continuous improvement of requirements, urban infrastructure construction is developing rapidly. Various underground pipelines and channels are increasing and the demand is increasing. As a trenchless technology, pipe jacking construction technology has been widely used in pipeline laying and underpass construction, especially in complex urban environments and cross-river regions, which has great advantages [1]. However, the pipe jacking machine may be resisted by underground obstacles in the construction process due to various reasons, such as the lack of reasonable planning of underground space development in the early stage, different structure forms of underground excavation support and foundation, complex geological conditions and etc. The underground obstacles include the foundation structures of existing buildings, support structures of underground excavation, abandoned structures, existing pipelines and solitary rocks. The pipe jacking machine crossing the stratum with obstacles will bring great risks, which will be a great challenge for the practice of pipe jacking engineering. The construction technology of pipe jacking through underground obstacles

---

*Corresponding Author:
Yue Zhao,
Science and Technology Service Platform, Qilu University of Technology (Shandong Academy of Sciences), Jinan, Shandong 250000, China;
Email: zhaoy@sdas.org

still needs further investigation.

The development of mechanical equipment and construction method of pipe jacking method mainly draws on the application experience of the shield method in the early period. Common shield tunneling machines and pipe jacking machines are usually only applicable to strata with little change in mechanical properties and do not have the function to remove obstacles in strata. For a slurry-balanced shield machine, a small crusher is equipped to ensure the smooth excavation of the mud suction pump, which can break small stones. When obstacles, such as reinforced concrete piles, underground diaphragm walls, or large solitary stones, are encountered on the tunnel or pipeline line, common shield tunneling machines and pipe jacking machines cannot pass through directly. In this case, adjusting the line position to avoid obstacles and structures is an economical and safe method. When the line cannot avoid obstacles, treatments such as removing existing structures, pulling piles on the ground, and removing obstacles after digging shafts could be used to remove the obstacles in advance. Subsequently, the pipe jacking machine could be jacked through this region. With the continuous improvement of the shield tunneling machine and pipe jacking machine technology, the cutting performance of the shield tunneling machine and pipe jacking machine has been continuously improved. Cases of direct-cutting obstacles have appeared in the past decade, such as the Shenzhen North Ring Line, Shanghai Metro Line 10, Suzhou Metro Line 2, etc. [2]. The mentioned cases are all practices of the shield method directly cutting underground obstacles. However, the cases of pipe jacking method are rare. Direct cutting of reinforced concrete structure has great wear to the cutter head. A large number of studies have made beneficial improvements to the performance of the shield cutter head, mainly by improving the configuration and performance of different types of cutters. For a pipe jacking tunnel, its diameter is often smaller than a shield tunnel, it is less difficult to directly cut obstacles.

Among the types of underground obstacles, the anchor cable structure is the most difficult one to deal with. Anchor cable is a kind of anchorage technology, which is often used as the support structure of underground excavation with a pile or diaphragm wall. The anchor cable structure is composed of grout and steel strand, which has a high tensile strength of 1860 MPa. Therefore, if the pipe jacking machine cuts the anchor cable structure directly, the cutter head could be wound due to the high toughness of the steel strand, which could cause damage to the pipe

jacking machine. At present, the common crossing method is to remove the existing anchor cable structure and then perform the pipe jacking method. When the space requirement is satisfied, the anchor cable can be directly pulled out at one end. However, this method has two disadvantages: 1) When the pull-out force is insufficient, the anchor cable cannot be pulled out (in this case, the casing follow-up method can be used to reduce the friction resistance between the anchor cable and the ground); 2) Corrosion of anchor cable structure causes the anchor tendon to break. Therefore, the method of directly pulling out the anchor cable is often unable to complete the removal of the anchor cable structure. In addition, a rotary drilling rig can be used to drill and remove the anchor cables. The rotary drilling rig has a high torsion force. Through torsion and winding, the steel strand could be taken out of the ground. However, this method needs a large workspace and has a rotary drilling workload. In addition, the anchor cable structure can be broken manually by excavating the existing anchor cable area. However, in the process of excavation, the construction of excavation support structures is the most difficulty of this method. Because of the existence of a steel strand, the water stop system of the supporting structure can not be continuous, resulting in waterproofing failure. Based on this, combining the steel-sheet piles and jet grouting piles for waterproofing and supporting excavation methods for crossing the anchor-cable area is proposed [3]. Through the occlusion of steel sheet piles and high-pressure jet grouting piles, waterproofing can be ensured in the process of excavation construction. The mentioned methods have been successfully applied in many case histories. When the surrounding environment is complex, the surrounding strata are often reinforced by grouting.

To sum up, some solutions to pipe jacking through different underground obstacles have been proposed. However, there is still great room for further improvement. Especially for the case of pipe jacking through the stratum of anchor cable structure, the construction technology is still complicated for professional persons. Therefore, more efforts are required to improve the mechanical properties of pipe jacking machines and study the obstacle removal methods.

Conflict of Interest

The authors declare that they have no known competing financial interests or personal relationships that could have appeared to influence the work reported in this paper.

References

[1] Li, T., Zhao, W., Liu, R., et al., 2021. Experimental study on the pipe-soil interface under the influence of pipe jacking stagnation time. KSCE Journal of Civil Engineering. 1-11.

[2] Xu, Q., Zhu, H., Ma, X., et al., 2015. A case history of shield tunnel crossing through group pile foundation of a road bridge with pile underpinning technologies in Shanghai. Tunnelling and Underground Space Technology. 45, 20-23.

[3] Han, J., Wang, J., Jia, D., et al., 2022. Construction technologies and mechanical effects of the pipe-jacking crossing anchor-cable group in soft stratum. Frontiers in Earth Science. DOI: https://doi.org/10.3389/feart.2022.1019801.

JAESER 2022 Reviewer Recognition and Thanks

JAESER would like to thank all the reviewers who spent their valuable time supporting the peer review process. We will continue to publish research related to the built environment and structural engineering and would like to thank all of our peer reviewers for their continued support and service to the journal and the broader scientific community

Outstanding Reviewer

Jian-yong Han   Northeastern University,China

Reviewer Acknowledgement

Marco Breccolotti   University of Perugia,Italy

Huaping Wang   Lanzhou University,China

Ahmed Elyamani Ali   Cairo University,Spain

Mohammed Jassam Altaee   University of Babylon,Iraq

Mª Dolores Álvarez Elipe   CEIPSO Salvador Dalí,Spain

Alper Bideci   Düzce University, turkey

Seongkyun Cho   Ministry Of Land,Infrastructure,and Transport, Republic of Korea

Fabrizio Scozzese   University of Camerino,Italy